Scenario development during commissioning operations on the National Spherical Torus Experiment Upgrade

To cite this article before publication: D J Battaglia *et al* 2018 *Nucl. Fusion* in press https://doi.org/10.1088/1741-4326/aaa6e0

Scenario Development During Commissioning Operations on the National Spherical Torus Experiment Upgrade

D.J. Battaglia[1], M.D. Boyer[1], S. Gerhardt[1], D. Mueller[1], C.E. Myers[1], W. Guttenfelder[1], J.E. Menard[1], S.A. Sabbagh[2], F. Scotti[3], F. Bedoya[4], R.E. Bell[1], J.W. Berkery[2], A. Diallo[1], N. Ferraro[1], S.M. Kaye[1], M.A. Jaworski[1], B.P. LeBlanc[1], M. Ono[1], J.-K. Park[1], M. Podesta[1], R. Raman[5], V. Soukhanovskii[3],
And the NSTX-U Research, Operations and Engineering Team

[1] Princeton Plasma Physics Laboratory
[2] Columbia University
[3] Lawrence Livermore National Laboratory
[4] University of Illinois at Urbana - Champaign
[5] University of Washington

The National Spherical Torus Experiment Upgrade (NSTX-U) will advance the physics basis required for achieving steady-state, high-beta, and high-confinement conditions in a tokamak by accessing high toroidal field (1 T) and plasma current (1.0 - 2.0 MA) in a low aspect ratio geometry (A = 1.6 - 1.8) with flexible auxiliary heating systems (12 MW NBI, 6 MW HHFW). This paper describes progress in the development of L- and H-mode discharge scenarios and the commissioning of operational tools in the first ten weeks of operation that enable the scientific mission of NSTX-U. Vacuum field calculations completed prior to operations supported the rapid development and optimization of inductive breakdown at different values of ohmic solenoid current. The toroidal magnetic field (B_{T0} = 0.65 T) exceeded the maximum values achieved on NSTX and novel long-pulse L-mode discharges with regular sawtooth activity exceeded the longest pulses produced on NSTX (t_{pulse} > 1.8s). The increased flux of the central solenoid facilitated the development of stationary L-mode discharges over a range of density and plasma current (I_p). H-mode discharges achieved similar levels of stored energy, confinement ($H_{98y,2}$ > 1) and stability ($\beta_N/\beta_{N\text{-nowall}}$ > 1) compared to NSTX discharges for $I_p \leq 1$ MA. High-performance H-mode scenarios require an L-H transition early in the I_p ramp-up phase in order to obtain low internal inductance (l_i) throughout the discharge, which is conducive to maintaining vertical stability at high elongation (κ > 2.2) and achieving long periods of MHD quiescent operations. The rapid progress in developing L- and H-mode scenarios in support of the scientific program was enabled by advances in real-time plasma control, efficient error field identification and correction, effective conditioning of the graphite wall and excellent diagnostic availability.

1. Introduction

On August 10, 2015 the first plasma discharge was formed in the National Spherical Torus Experiment Upgrade (NSTX-U) at the Princeton Plasma Physics Laboratory (PPPL) in Princeton, NJ. The inaugural discharge marked the completion of a multi-year upgrade of the NSTX experiment aimed at extending the performance of magnetic confinement of high-temperature plasmas in a low-aspect ratio toroidal geometry.

A primary mission of the NSTX-U experiment is to access unique confinement regimes and enable critical studies that will identify the aspect ratio of next-step magnetic confinement reactor-scale devices. This mission builds on the results from the NSTX (operated from 1999 to 2010) [1,2] by extending the plasma discharge pulse length about a factor of five and nearly doubling the strength of the toroidal magnetic field (B_T), plasma current (I_p) and neutral beam injection (NBI) heating power in a low-aspect ratio toroidal confinement configuration [3, 4, 5]. These new capabilities expand the regimes available for scientific discovery in the low-aspect-ratio spherical tokamak (ST) configuration by providing access to lower-collisionality plasmas and larger fractions of non-inductive current drive that bridge the gap in the performance of NSTX and the conditions required for a steady-state device designed to study nuclear science [6] or the generation of fusion power [7]. These plasma regimes also approach the conditions achieved on conventional aspect ratio tokamaks with a comparable plasma cross-section, such as DIII-D and ASDEX-Upgrade, providing an opportunity to test and validate plasma physics models used to optimize future burning-plasma devices such as ITER.

One major element of the upgrade to NSTX was the installation of a center-stack (CS) with a larger diameter, increasing the aspect ratio of the device from 1.4 to 1.7. The larger diameter CS supports an increase in the maximum on-axis toroidal field strength from 0.55 T on NSTX to 1.0 T on NSTX-U and a factor-of-three increase in the volt-seconds available for inductive current from the ohmic (OH) solenoid coil. The second major element of the upgrade was the addition of a neutral beam with three separate sources, doubling the available neutral beam heating power. The three new beamlines inject at a larger tangency radius than the three existing beam lines, significantly increasing the neutral beam current drive capabilities and expanding the actuators available for real-time current and rotation profile control [8, 9, 10]. Initial studies on NSTX-U have also demonstrated the suppression of fast-ion driven instabilities when using the new more-tangential neutral beam injection [11].

The number and position of the divertor coils were changed for NSTX-U to improve the flexibility in the divertor topology in both single-null and double-null

shapes. Most notably, the coils are up-down symmetric to allow for advanced divertor topologies, such as the snowflake configuration [12], to mitigate heat flux in both the upper and lower divertor. Operations at large I_p and heating power on NSTX-U may challenge limits to the plasma facing components (PFCs) in the divertor, placing increased emphasis on integrated solutions for divertor control and heat flux mitigation in high-performance scenarios. The available heating power and pulse length in the low-aspect ratio geometry makes NSTX-U well suited for developing and testing solutions for the plasma-material interface in future burning-plasma devices.

The initial operational period on NSTX-U was dedicated to commissioning activities aimed at developing plasma discharge scenarios, real-time control and plasma diagnostics needed to support the first experimental campaign on NSTX-U. Six discharge scenario milestones were established for the commissioning phase:
(1) inductive startup to $I_p = 0.2$ MA over a range of ohmic precharge ($I_{OH} = 8 – 20$ kA) and toroidal field ($B_T = 0.4 – 0.65$ T),
(2) inner-wall limited ramp-up and sustainment with $I_p \geq 0.5$ MA, $t_{flattop} \geq 0.5$ s and $B_T = 0.4 – 0.65$ T,
(3) long-pulse, diverted beam-heated L-mode with $I_p \geq 0.5$ MA, $t_{flattop} \geq 1.0$ s and $B_T = 0.4 – 0.65$ T,
(4) high-current, diverted beam-heated L-mode with $I_p \geq 1.0$ MA, $B_T = 0.65$ T,
(5) ELM-ing H-mode fiducial with $B_T = 0.65$ T, $I_p \geq 1.2$ MA, $t_{flattop} \geq 0.5$ s, and periods free of MHD activity, and
(6) an NSTX-like ELM-ing H-mode fiducial with $B_T = 0.45$ T, $I_p = 0.9$ MA, $t_{flattop} \geq 0.5$ s, and periods free of MHD activity.
These scenarios enable experiments that could scan parameters to touch base with NSTX results and leverage the new capabilities of NSTX-U, such as the more tangential neutral beam lines, new double-null divertor configurations, longer pulse lengths and larger B_T.

NSTX-U commissioning operations began in December 2015 and concluded in June of 2016 after completing nearly 90% of the planned tasks. Operations ended prematurely due to an internal short within a divertor poloidal field coil that necessitated repair. Ten weeks of operations were completed with each week consisting of about 100 discharges on average. Every two weeks of operation was followed by a maintenance period lasting 2 – 4 weeks. The inner-wall limited and long-pulse L-mode scenario targets were demonstrated within the first two weeks of operations enabling rapid progress in error field identification and correction, axisymmetric plasma shape control development and diagnostic systems commissioning. These activities, in turn, enabled steady progress toward the development of a high-current L-mode discharge and high-performance H-mode scenarios. H-mode discharges with MHD-free periods, regular ELMs and flattops exceeding 0.5s with $B_T > 0.6$ T were developed, however the target I_p

(1.2 MA) was not achieved prior to the premature conclusion of operations. Furthermore, no attempts were made to produce H-mode discharges at lower B_T that were required for experiments to make a connection to NSTX operations.

A recent publication summarizes the primary physics results of the commissioning phase of NSTX-U [13]. This companion paper provides greater detail on the modeling and scenario development that enabled the first physics results. The diagnostic and control capabilities of NSTX-U during the commissioning phase are summarized in Section 2. Section 3 describes the wall conditioning employed on NSTX-U and describes the impact of wall conditioning on the plasma performance. The next three sections provide detail on the plasma startup (section 4), development of long pulse and high-current L-mode discharges (section 5) and high-performance H-mode discharges (section 6). The final section presents a summary and future plans for scenario development on NSTX-U.

2. NSTX-U configuration for the commissioning phase

2.1 Magnetic field coil control and protection

Figure 1 shows a poloidal cross-section of the NSTX-U vacuum vessel and poloidal field (PF) coils. The direction of toroidal magnetic field is out of the page while the toroidal plasma current is into the page. Flux surface contours for an H-mode discharge are shown in gray. The PF5 coil set consists of two coils, above and below the midplane, wired in series and powered by a unipolar power supply (current direction is opposite I_p). This coil set provides the confining vertical field necessary to maintain a requested outer gap, i.e. the distance between the plasma boundary and the outboard limiter. Two bi-polar power supplies independently power the PF3U and PF3L coils, which are used to form a poloidal field null for breakdown, control the plasma height and squareness and maintain the vertical position of the plasma via active vertical position feedback control. The PF2U, PF2L, PF1AU, and PF1AL divertor coils each have a dedicated unipolar power supply that provides a diverting field (opposite polarity to PF5). The PF4, PF1B and PF1C coil sets were not used in plasma discharges during commissioning operations. Variable dc voltage is applied to the TF, ohmic solenoid (OH) and PF coils by separate thyristor rectifier power suplies for each coil [14]. NSTX-U retained six window-pane coils from NSTX (referred to as the resistive wall mode or RWM coils) that circle the midplane of the device and are close fitting to the outside of the vacuum vessel [15]. These coils are used to provide error-field correction and suppression of RWM instabilities. Each of the six coils is driven by a dedicated subunit of a Switching Power Amplifier (SPA) [16].

Figure 1 also shows the tangency plane for the six co-I_p neutral beams. The three beams at the innermost radii come from a single beam box that operated on NSTX. The other three beams originate from a second beam box that was added as part of the upgrade. Each separate beam is capable of injecting 2 MW when operating at 90 kV [3] The neutral beams were conditioned in parallel with commissioning operations, increasing the aggregate power heating power available from 3 MW in the second week to 12 MW soon after the conclusion of plasma operations. The higher-harmonic fast wave (HHFW) antenna (shown as red lines within the outboard midplane boron nitride (BN) limiter in figure 1) was conditioned in vacuum during commissioning operations in preparation for dedicated experiments planned for the scientific campaign.

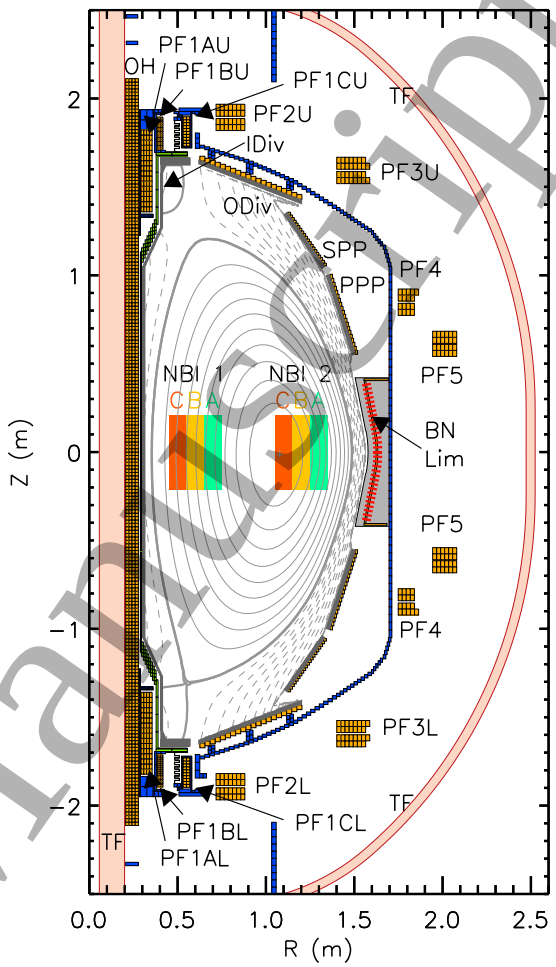

Fig 1 Cross section of NSTX-U showing the poloidal field coils (PF), ohmic solenoid (OH), toroidal field coil (TF), boron nitride (BN) limiter and tangency plane of six neutral beams (colored rectangles). The inboard and outboard divertors (IDiv and ODiv), and secondary and primary passive plates (SPP and PPP) are labeled in the upper half and repeated in the lower half of the device. Gray contours show flux surfaces for discharge 204112 at 0.8s.

NSTX-U has twelve toroidal field coils with three turns per coil. A cross section of a single TF coil leg is shown in figure 1. The inner and outer legs of the TF conductors are connected with flexible joints at both the top and bottom of the device [3]. The OH coil is wrapped around the TF conductors and are maintained at a larger temperature than the TF conductors to ensure the radial thermal expansion of the inner diameter of the OH windings exceeds the radial expansion of the TF inner legs. The upgraded device is designed to operate with toroidal field coil current up to 130 kA per turn (giving 4.68 MA rod current) in order to produce a 1 T magnetic field at R = 0.936 m. The central solenoid is designed for a maximum current of 24 kA in both polarities. Commissioning of NSTX-U was completed at reduced fields to provide an opportunity to evaluate the structural models used for the new design in a safe operating range while permitting field and pulse durations that exceeded the conditions achieved on NSTX. The maximum toroidal field

current in the commissioning phase was 84.5 kA, which produced an on-axis toroidal field (0.65T) that exceeded the maximum on-axis toroidal field achieved on NSTX (0.55T). The solenoid current magnitude was limited to 20 kA or an ohmic flux of 1.6 Wb, which is about double the ohmic flux available on NSTX (0.75 Wb).

One significant commissioning task was the deployment of the Digital Coil Protection System (DCPS) [17]. The DCPS computes about 400 real-time force, stress and heating calculations using measurements of the coil and plasma currents. Additionally, the calculations consider the worse-case forces that are induced by the immediate quench of the plasma current during a disruption event. If any of the instantaneous or estimated disruption force, stress or heating calculations exceed a prescribed threshold, all of the power supply rectifiers are placed in "suppress and bypass" mode where the high voltage is removed and all coil currents decay with a characteristic L/R decay. The heating calculations include an estimate for the heating that will occur during the current decay in order to ensure the threshold in the coil heating is not exceeded during suppress and bypass. The system is designed for every shot protection by integrating redundant calculations with multiple layers of system status checking and fault detection. The DCPS replaces the NSTX protection system that limited the coil current and pulse duration to ensure operations remained below all force, stress and heating limits; this conservative method of protection was too restrictive to the operational space anticipated for NSTX-U. The DCPS system was active for all discharges in the commissioning campaign and demonstrated routine effectiveness in protecting the mechanical systems against a variety of potentially harmful conditions, including the loss of real-time control communication, an incorrect configuration of the coil power supplies, and approaching the coil heating and force limits. The force and heating limits for the commissioning phase were chosen to be at or below 80% of the design fatigue limit in order to ensure operation remained in a safe operating regime while the device monitoring and protection systems were evaluated.

The Plasma Control System (PCS) on NSTX-U contains an infrastructure of hardware and software designed to control aspects of the plasma discharge in real time, including the plasma current (I_p), poloidal cross-section shape, neutral beam injection and gas fueling. The plasma shape and I_p are inferred using a large set of magnetic sensors, and the ohmic solenoid and poloidal field coil currents are adjusted in real-time to achieve the programmed targets. Most of the PCS hardware and software was modified during the upgrade construction period to significantly improve the capabilities of the system, especially concerning the ability to easily expand the volume of real-time inputs and the complexity of the real-time calculations [18].

2.2 Plasma Diagnostics

Rapid progress in discharge development on NSTX-U was enabled by the availability of many plasma diagnostics through the entire commissioning phase. A full set of magnetic field and flux measurements, including the expanded diagnostic set on the new center column and a new diamagnetic flux measurement system, were commissioned and calibrated within the first several days of the commissioning campaign [19]. Magnetic signal integrators were calibrated using a dedicated test stand, while the sensors were calibrated and corrected for spurious pickup using single coil test shots. These activities also refined the conductive wall model used in EFIT and LRDFIT (LR circuit model with Data FITing capabilities) to support calculations of the vacuum field and plasma equilibrium. Between shot plasma equilibrium calculations using the calibrated magnetics (EFIT01) [20] were available for all discharges, and a between-shot partially-kinetic equilibrium calculation that incorporates the diamagnetic flux measurement and electron profiles (EFIT02) [21] was available following a few weeks of operation.

The 42 channel Multi-pulse Thomson Scattering (MPTS) system provides measurement of the electron temperature and density profiles on the midplane. The system documents both sides of the magnetic axis and the scrape-off layers (SOL). MPTS underwent major modifications to accommodate the larger diameter of the center stack and avoid the second neutral beam line [22]. Measurements from the diagnostic were available on the first day of operations and between-shot data was provided reliably through the initial campaign.

Future operations on NSTX-U will have MPTS measurements available to the real-time plasma control system in order to support a variety of control algorithms and add additional constraints on the real-time plasma equilibrium calculations. NSTX-U will also add a multi-chord far infrared (FIR) interformeter system for measuring the electron density in real-time. The interferometer and real-time MPTS (rtMTPS) system will provide an opportunity for real-time density feedback control. However, similar to NSTX, the first operation of NSTX-U did not have real-time density measurements to support active density control.

A suite of charge-exchange recombination spectroscopy (CHERS) diagnostics provides profiles of the carbon ion temperature, density and rotation when using neutral beam injection [23] and an edge Doppler spectroscopy diagnostic. Between-shot analysis was available for the toroidal views of the standard CHERS using C VI spectroscopy and the Edge Rotation Diagnostic (ERD) [24] that utilizes spectroscopy of C III. In addition, the new real-time velocity measurement system was commissioned [25], which provides higher time-resolved toroidal velocity measurements at reduced profile resolution to the real-time plasma control system to support on-going research into active control of the

plasma rotation. Poloidal views of the standard CHERS diagnostic can provide poloidal velocity measurements along the midplane of NSTX-U [26].

One potential challenge for the CHERS systems on NSTX-U is that the new neutral beam lines intersect the views of the passive viewing system dedicated to compensating the active views. As a result, CHERS analysis was only available when only the original beam lines was injecting (NBI 1). An experiment performed in the commissioning campaign demonstrated that beam modulation scenarios could be used to obtain CHERS profiles in experiments using the second beamline (NBI 2). In all of the beam-modulation scenarios, the passive emission is inferred by subtracting two phases of the modulation. Thus, this technique is applicable to time periods where the discharge is relatively stationary over the modulation period (typically 40 ms).

A suite of volume-integrated and spatially resolved spectroscopic diagnostics supported operations, especially in the monitoring of wall conditions. The volume-integrated views had dedicated filterscopes for visible spectroscopy lines (D_α, D_γ, C II, C III, B II, Li I, O II, He II) and a survey spectrometer (VIPS) that can be tuned to a wavelength range of interest [27]. One utility of the VIPS diagnostic is resolving the relative D_α and H_α brightness during a discharge as a measure of the relative concentration of hydrogen neutrals to deuterium neutrals. This measurement can provide a tool for quantifying the source of hydrogen from water liberated from the graphite tiles.

Spatially resolved full poloidal/toroidal coverage of impurity emission from the PFCs was achieved in NSTX-U via bandpass-filtered 2D fast cameras viewing the upper and lower divertor. Two wide-angle fast visible cameras from NSTX were reinstalled for the full toroidal imaging of the lower divertor [28] and two new cameras added a symmetric view of the upper divertor. The wide-angle cameras were dedicated to deuterium and carbon emission measurements in the initial NSTX-U experimental campaign. Two dual-wavelength imaging systems TWICE-I and TWICE-II (Two Wavelength Imaging Camera Equipment) [29], based on a charge injection device (CID) radiation-hardened intensified camera, complemented fast cameras imaging capabilities with the ability to image weaker visible lines and provided a two-color system for the simultaneous imaging of different wavelengths. In the initial NSTX-U experimental campaign, TWICE-I and TWICE-II were dedicated to the monitoring of oxygen, boron and molecular carbon emission from the lower divertor.

The chemical composition of the surface layers of the first wall has a large impact on the performance of a discharge. The Materials Analysis and Particle Probe (MAPP) is a novel diagnostic that quantifies the first wall surface chemistry during plasma exposure, wall conditioning and long periods under vacuum [30]. The diagnostic has an array of

material samples that are positioned flush with first wall surface of the lower divertor. The samples can be retracted into an analysis chamber where X-ray photoelectron spectroscopy (XPS) is conducted in the chamber to characterize the material composition within the top 20 nm of each sample. The XPS analysis was performed at the conclusion of each run day during the commissioning period, and the capability to perform this analysis between shots is in development for future operations.

Operations on NSTX-U relied on visible fast camera imaging to provide confirmation of the plasma position within the vacuum vessel, the timing of plasma breakdown and gas fueling, the timing of transitions into and out of H-mode and qualitative measurements of the wall conditions and impurity sources. The production of neutrons from DD fusion was monitored using fission chamber and scintillator neutron detectors. Operations were also supported by BEtween and Among Shot TRANSP analysis (BEAST) that provides information on the neutral beam heating and current drive efficiency throughout the discharge by incorporating the available magnetic, profile and neutron diagnostics in the interpretative calculations.

In addition, a number of diagnostics provided preliminary data or supported targeted experiments, such as:

- The core and edge tangential Multi-energy Soft X-ray (ME-SXR) system for high time resolution measurements of the electron temperature [31]
- The midplane tangential Transmission Grating Imaging Spectrometer (TGIS) for impurity studies [32]
- The poloidal Ultrasoft X-ray (USXR) arrays for MHD mode detection, the Lyman Alpha Diode Array for imaging the divertor radiation [33]
- A new fast camera with higher sensitivity and optimized throughput enabled imaging of divertor turbulence via C III emission.
- The Synthetic Aperture Microwave Imaging (SAMI) diagnostic that measures the magnetic field pitch in the plasma edge [34]
- An expanded Beam-Emission Spectroscopy (BES) diagnostic for spatially-resolved measurements of longer wavelength density fluctuations
- A suite of high spectral resolution extreme ultraviolet (EUV) grating spectrometers used to infer impurity densities [35]
- The ENDD diagnostic (Edge Neutral density Diagnostic) [36] provides a measurement of the D-α emission shell to determine neutral densities at the LFS midplane. The diagnostic was upgraded with a new imaging setup based on a coherent fiber bundle in a re-entrant viewport.
- Vertically and tangentially viewing Fast Ion D-alpha (FIDA) diagnostics for evaluating the properties and density of fast ions

- A multi-view Solid State Neutral Particle Analyzer (SSNPA) [37], and
- The scintillator-based Fast Lost Ion Probe (sFLIP) to measure the energy and pitch of fast ions lost to the wall

Measurement of the internal magnetic field pitch is an important constraint on the q-profile in equilibrium reconstructions. The Motional Stark Effect (MSE) diagnostic from NSTX was retained for NSTX-U to provide this measurement. The diagnostic is designed to image the plasma along the neutral beam 1A injection with the beam voltage at 90 keV. The 1A neutral beam was not conditioned to 90 keV until the final week of the commissioning period and the MSE diagnostic did not have an opportunity to collect calibrated data in this campaign. A laser induced florescence (LIF) MSE diagnostic was installed on NSTX-U to provide an additional constraint to the current profile in the H-mode pedestal. This diagnostic relies on a diagnostic neutral beam, which was tested, but not fully commissioned during the ten weeks of operations.

3. Wall conditioning

High-performance discharges in tokamak devices require the mitigation of impurity contamination of the confined plasma from the PFCs. The majority of the wall tiles on NSTX-U are constructed of the same isotropic graphite material as NSTX. It is necessary to heat (i.e. bake) these materials prior to plasma operations in order to accelerate the migration of water trapped within the material lattice to the surface where it can be released into the vessel and be pumped away. The NSTX-U tiles were held at an elevated temperature for three weeks while the vessel was under vacuum. The outboard divertor (ODiv in figure 1) and passive plate (SPP and PPP in figure 1) tiles are heated using a 350° C flowing helium system. Thermocouple measurements indicate the outboard divertor plates and passive plates achieved temperatures at or above 320° C. The direction of the helium flow was reversed mid-way through the baking period to balance the heating to the surfaces along the heating loop.

The inboard wall tiles are heated via dc current to a target temperature of 350° C and the vertical section of the inboard divertor (IDiv in figure 1) to 320° C. The horizontal section of the IDiv was heated via conduction from the central column, however it only achieved temperatures around 220° C. The low bake temperature was due to large heat conduction to the PF1B coil support structures that were actively cooled to maintain the PF1B coil at a safe temperature. Consequently, the tiles within horizontal section of the IDiv are suspected to be the largest source of water in the vessel during plasma operations. The limit on the baking temperature of these tiles will be increased for future operations following design changes to the divertor regions.

Boronization is a proven technique for reducing the oxygen content of plasmas in tokamaks with carbon tiles whereby a thin layer of boron is applied to the tile surface to trap water below the coating and react with liberated oxygen. The thin layer is replenished periodically without breaking vacuum via a plasma glow discharge. On NSTX-U, the boronization glow discharge is conducted using a mixture of 95% helium and 5% deuterated trimethylborane (dTMB). The injection location for the dTMB gas was increased from a single midplane gas valve on NSTX to three valves (top, bottom and midplane) in order to facilitate experiments on boron deposition [38]. A traditional boronization scheme for NSTX-U is to conduct eight hours of a boronization glow, followed by a shorter period of pure helium glow to liberate the deuterium that was co-deposited on the graphite tiles. During plasma operations, helium glow discharge cleaning (GDC) is utilized to reduce the deuterium inventory in the tiles prior to each discharge. Approximately thirty minutes of helium GDC is performed at the start of the run day and about ten minutes of GDC is performed prior to each shot.

The first two and half days of the commissioning period were dedicated to establishing inner-wall limited (IWL) discharges following the full vessel bake, but before to the first boronization. The retention of deuterium in the graphite tiles was reduced using helium glow discharges between shots. Furthermore, the initial plasma breakdown was achieved in deuterium, however the plasma was fuelled during the discharge with helium to minimize deuterium retention in the tiles. These early discharges achieved suitable length such that it was possible to establish active feedback of the plasma current, outer boundary gaps and vertical position. These tools produced stable IWL discharges at I_p = 500 kA that terminated when the ohmic solenoid current reached the prescribed limit of -19kA, as shown in figure 2. Repeat discharges conducted following the first boronization demonstrated that oxygen content of the IWL discharges was reduced as measured by a filterscope with a radial field of view at the midplane (figure 2). The reduction in the oxygen content resulted in an increase in the length and stored energy of the otherwise matched discharge.

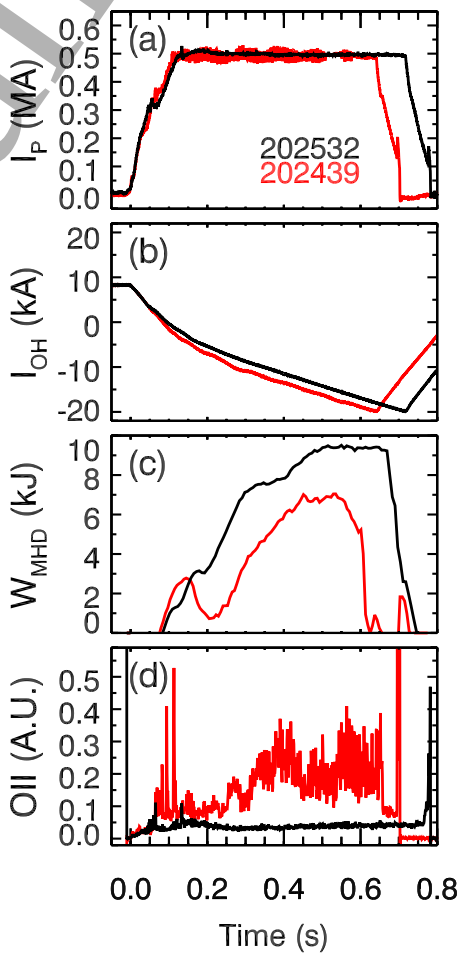

Fig 2 Comparison of matched discharges before (red) and after (black) the first boronization on NSTX-U.

Two different boronization strategies were employed during the commissioning period in order to reduce the impurity content of the plasma. In the first seven run weeks, an eight-hour boronization using a full bottle of dTMB was completed about once per run week. In the final three run weeks, two-hour boronizations using only about one-fifth of a bottle (referred to as mini-boronizations) were completed every one or two run days. The two-hour boronizations were performed during evening hours when maintenance, installation and operation activities would normally not occur, increasing the efficiency of the commissioning activities. The mini-boronization resulted in a boron layer in the lower outboard divertor that was thinner (~ 1.5 nm) than the layer deposited with a full-boronization (> 20 nm) as measured by the MAPP probe. The frequent application of thin boron layers was effective at maintaining the wall conditions at reasonable levels, however the oxygen content within the surface layer of the tiles following a mini-boronization was observed to increase more rapidly compared to a full-boronization when plotted versus an estimate for the particle fluence to the divertor surfaces [38]. The more rapid change in the wall conditions hindered the development of repeatable H-mode discharge scenarios, as discussed in section 6.

Spectroscopic measurements of matched low-power discharges performed immediately following full- and mini-boronizations provided guidance on the state of the wall conditions during commissioning operations. Measurements from the VIPS spectrometer indicated the ratio of neutral hydrogen compared to the total neutral hydrogen and deuterium (i.e. H/(H+D)) in the upper and lower divertor was reduced to below 3% after the fourth full-boronization completed in the fifth week of operations. This hydrogen content was comparable to the values measured during scientific operations on NSTX and was restored following each full- and mini-boronization conducted during the final weeks of commissioning operations. However, the degradation of the good wall conditions following either type of boronization occurred much faster on NSTX-U than NSTX. For example, the H/(H+D) metric could increase about 1% over the course of about twenty high-power (P_{NBI} > 3 MW) discharges on NSTX-U, whereas NSTX could execute hundreds of discharges before observing a similar change. Consequently, the number and frequency of boronizations was larger in the NSTX-U commissioning period compared to comparable commissioning periods on NSTX. No concurrent rise in the nitrogen content was observed with the evolution of the hydrogen and oxygen content, indicating that the source was trapped water within the graphite tiles as opposed to an air leak into the vessel.

The fastest degradation of the wall conditions was observed following discharges with neutral beam heating above 1 MW. This is illustrated in figure 3 where the evolution of wall condition metrics are shown for two consecutive days following a mini-

boronization during the final week of the commissioning period. The first ten discharges on June 22 were short (< 0.5 s) H-mode discharges with P_{NBI} up to 6 MW; the remainder of the discharges on June 22 and 23 were longer duration (0.5 - 1.5 s) L-mode discharges with P_{NBI} = 1 MW. The vertical dotted line indicates the transition from H-mode to L-mode experiments, while the vertical dashed line indicates the transition between separate run days. Both the H- and L-mode discharges had a similar LSN, low elongation shape that placed the outer strike point on the outboard divertor target during flattop (see figure 10 as an example).

The square data points in figure 3 show the relative concentration of neutral hydrogen compared to total neutral deuterium and hydrogen using data from the VIPS spectrometer (data points for some discharges are missing when the spectrometer is tuned to different wavelengths) by averaging the ratios for the upper and lower divertor views. The diamond data points show the ratio of the O II and D_γ signals from filterscopes viewing vertically through the plasma toward the lower divertor. This ratio provides a relative metric of the oxygen content of the tile surfaces. Both ratios shown are the average values from 120ms – 180ms within each discharge, when the plasma is inboard limited and the details of the plasma are relatively independent of the experiment.

The lines connecting the diamonds in figure 3 illustrate that the details of the termination of a discharge impacted the wall conditions at the start of the next discharge. Discharges that ended with a vertical disruption event (VDE) generally led to a degradation of the wall conditions, especially in high-power H-mode discharges (black points). The green diamonds mark the low (1 MW) and high (> 1 MW) power discharges that ended without a VDE. The relative oxygen and hydrogen content is typically lower on the following shot (the green lines slant downwards). This lower value indicates that only heating the inboard limiter and outboard divertor targets (surfaces that were adequately baked) resulted in a net removal of impurities from those surfaces. The orange and black points indicate discharges that

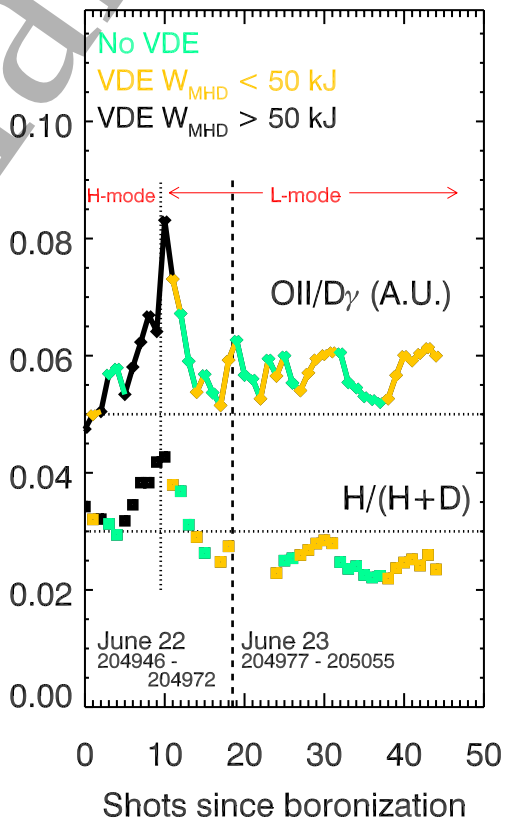

Fig 3 Evolution of relative oxygen and hydrogen impurity content following a boronization. The evolution of the wall conditions depends on the heating of the divertor PFCs due to VDEs.

ended with a VDE. Generally, the impurity content is larger following these discharges and scales with the size of the stored energy (W_{MHD}) lost during a VDE. The notable exceptions are the first two long L-mode discharges where the beneficial scrubbing of the outboard divertor and inner limiter by the plasma outweighs the detriment of the VDE.

Operations during the L-mode discharges demonstrate that avoiding heating the inner divertor by not placing a strikepoint on these surfaces and keeping the energy deposited in the divertor during a VDE below 50 kJ maintains the plasma impurity content at a level comparable to the conditions achieved right after the boronization. The relative hydrogen content (squares) is reduced over the course of the L-mode discharges as they result in minimal heating of the inboard divertor tiles. The impurity content of discharges at the start of the second day (June 23) is similar to the last shot of the previous day. This supports the thesis that the source of oxygen and hydrogen is not a leak in the vacuum vessel, but rather water trapped within material surfaces. The rapid increase in the oxygen and hydrogen content during the first ten discharges in figure 3 was consistently observed whenever a series of high-power discharges were conducted. This presented an operational challenge when developing high-performance H-mode scenarios and will be discussed in more detail in section 6.

The intention of the commissioning campaign was to establish long-pulse L- and H-mode discharges with boron wall conditioning before switching to lithium wall conditioning to provide a quantitative comparison between the two wall conditioning techniques. NSTX observed a favorable reduction in deuterium recycling content via the application of thin solid lithium coatings to the carbon tiles using a lithium evaporator [39]. The longer pulse discharges afforded by the upgrade would investigate if the benefits of lithium conditioning persisted through a longer discharge. The premature end of the first campaign did not allow for the program to begin lithium wall conditioning, however some dedicated lithium spectroscopy diagnostics were qualified due to the presence of trace amounts of lithium remaining on tiles used in NSTX operations.

4. Plasma Discharge Startup

The inductive startup procedure on NSTX had to be modified for NSTX-U due to the increased diameter of the center-stack and changes to the conductive elements in the wall and support structure. Therefore, calculations were performed prior to NSTX-U operations in order to develop procedures for independently scanning the breakdown timing, target loop voltage and ohmic solenoid precharge current to support the efficient development of startup scenarios. The calculations were completed using LRDFIT, a time-dependent axisymmetric magnetic field solver with realistic toroidal conductive elements. The model was first used to evaluate a typical NSTX startup scenario to

provide a reference case for comparison to NSTX-U predictions. The inductance and resistance of the NSTX structural elements used in the axisymmetric model were well constrained by both measurements and modeling.

Figure 4 shows the current in the ohmic solenoid, PF3 and PF5 coils for a typical inductive startup on NSTX (black traces). The ohmic solenoid (figure 4a) is pre-charged to an initial positive current (24 kA) and the fringing or stray field from the solenoid introduces a vertical magnetic field within the vacuum chamber (downward, the confining direction). Unlike some devices that have a dedicated poloidal field coil set for excluding (i.e. cancelling) the ohmic fringe field, such as DIII-D [40], NSTX-U employs the PF3 coil set to cancel (i.e. null) the poloidal magnetic field from the solenoid in a localized region during the breakdown phase. This requires the current in both PF3 coils to be positive prior to the discharge, then ramp to a negative current following the breakdown phase in order to contribute to the confining vertical field (figure 4b). The rapid change in the PF3 current is facilitated by 2 kV power supplies that drive the upper and lower PF3 coils. The PF5 coils (figure 4c) near the outboard midplane contribute to the vertical confining field following breakdown.

Results from JET and DIII-D indicate that reliable inductive startup of a plasma discharge without electron-cyclotron (EC) pre-ionization requires $E_\phi B_\phi / \langle B_\theta \rangle > 1$ kV/m where $\langle B_\theta \rangle$ is the average poloidal field within a toroidal annulus [40, 41] and $E_\phi = V_{loop}/2\pi R$. This expression can be restated as

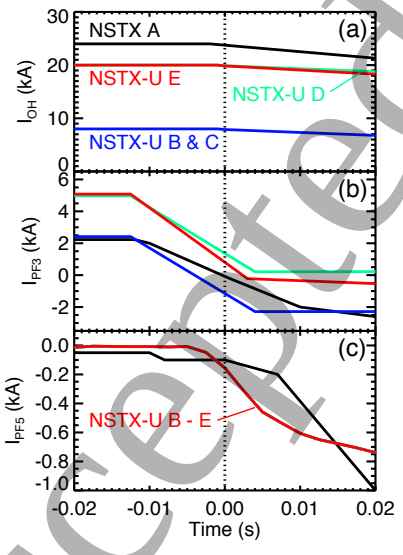

Fig 4 (a) Ohmic solenoid, (b) PF3 and (c) PF5 coil currents for the five models presented in figure 4.

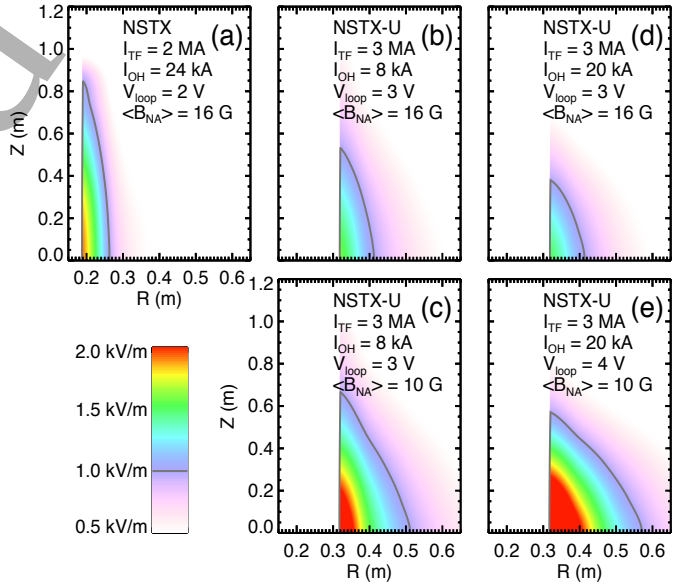

Fig 5 (a – e) Contours of the breakdown parameter (eq. 1) averaged over 2 ms in the time-dependent calculation for (a) NSTX and (b-e) NSTX-U.

$$\frac{V_{loop} I_{TF}}{10\pi R^2 \left(B_\theta + \langle B_{\theta,NA} \rangle\right)} > 1 \frac{\text{kV}}{\text{m}} \qquad \text{(Eq 1)}$$

where I_{TF} is the toroidal field coil rod current in MA, R is the major radius of the breakdown region in meters, V_{loop} is the loop voltage applied to the plasma in Volts, B_θ is the axisymmetric poloidal magnetic field and $\langle B_{\theta,NA} \rangle$ is the static toroidal average of the non-axisymmetric component of the poloidal magnetic field (i.e error field) in Tesla. The scaling of the expression on the left side of equation 1 is useful for relative studies in a constrained dataset with consistent choices of time and spatial averaging of the fields.

Figure 5a shows a calculation of the breakdown parameter given in equation 1 for NSTX where the fields are averaged over two milliseconds, which constitutes the first half of the observed avalanche phase (i.e. the period when D_α emission is increasing). Note that the calculation is symmetric about the midplane and only the top half of the breakdown region is shown. It is assumed that the root-mean-squared of n = 1 error field amplitude ($\langle B_{\theta,NA} \rangle$) at R = 0.3 m is 16 Gauss. This is consistent with measurements and modeling of the n = 1 error field amplitude due to the tilting of the toroidal field coil at maximum ohmic solenoid current, which was the dominant error field source at breakdown on NSTX [42]. The calculations are consistent with the observation from visible camera imaging that the breakdown region was close the inner wall and had a much larger vertical extent than radial extent. The time-averaged fields produce a breakdown parameter is on the order of the empirical breakdown requirement that $E_\phi B_\phi / \langle B_\theta \rangle > 1$ kV/m and the maximum instantaneous values for equation 1 are achieved around t = + 1 ms, indicating the model captures the timing of the field null.

Extending the semi-quantitative analysis to NSTX-U prior to operations required an estimate of the resistance of the conducting structures based on the material properties of each component. Recognizing that the resistance estimates introduce systematic errors, the model was used for qualitative studies in order to develop a recipe for changing the loop voltage, null timing and ohmic solenoid precharge. For each choice of I_{OH} precharge and V_{loop}, the I_{PF3} evolution prior to t = 0 is tailored to form a poloidal field null at R = 0.3 m at t = 0 (figure 4b). The start of the current ramp in I_{PF3} is held fixed at t = -15 ms while the start of I_{PF5} ramp begins at t = -5 ms (figure 4c). The evolution of the PF3 and PF5 current in the NSTX-U models was chosen to achieve a similar evolution of the plasma field curvature (i.e. field index) as NSTX in order to maximize the plasma elongation while remaining vertical stable without active feedback on the plasma position [43]. For simplicity, the PF5 current was the same for all NSTX-U calculations.

The major radius (R) of the breakdown region on NSTX-U is about 70% larger compared to NSTX (0.34 m compared to 0.2 m) due to the larger centerstack diameter. This leads to a factor of three increase in the V_{loop} requirement to achieve a similar breakdown metric (eq 1). However, NSTX-U is able to operate at larger I_{TF}, which acts to reduce the V_{loop} requirement. Figure 5b shows a calculation for NSTX-U using an I_{OH} precharge of 8kA, I_{TF} equal to 3.0 MA, and assuming the same value of $\langle B_{\theta,NA} \rangle$ used in the NSTX calculations (16 G). NSTX typically used an I_{OH} precharge of 24 kA, thus an 8 kA precharge on NSTX-U produces a comparable magnitude of the ohmic fringe field due to the fact that the cross-sectional area of the ohmic solenoid is about three times larger. The V_{loop} is 3V, which is close to the value realized in NSTX-U operations (2.8 V). The results of the calculation indicate the shape of the breakdown region has a smaller vertical extent, but larger radial extent compared to NSTX. The maximum magnitude of the breakdown metric is smaller in figure 5b compared to 5a when using a matched assumption for $\langle B_{\theta,NA} \rangle$. Figure 5c illustrates that the maximum of the breakdown parameter calculated for NSTX is recovered if the magnitude of the error field RMS is reduced by about 40%. This difference in $\langle B_{\theta,NA} \rangle$ is consistent with the experimentally observed loop voltage requirements on NSTX (2 V) and NSTX-U (3 V). This result suggests that n = 1 error field at the time of breakdown may be lower on NSTX-U than NSTX.

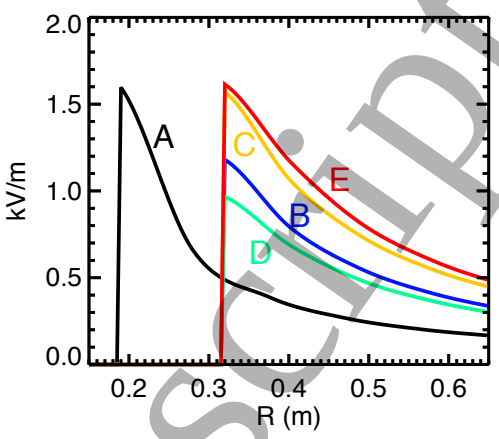

Fig 6 Average breakdown parameter between z = -0.8 m to +0.8 m versus major radius for each model case. Colors correspond to the model cases in figure 5.

Operations on NSTX-U ran with an I_{OH} precharge as large as 20 kA. The magnitude of the spatial gradients in the poloidal magnetic field is proportional to the coil currents, thus the vertical extent of the null region becomes smaller at larger precharge values. This is demonstrated in Figure 5d, where the same I_{TF}, V_{loop} and $\langle B_{\theta,NA} \rangle$ are used as Figure 5b, with the I_{OH} and I_{PF3} precharge levels increased by about a factor of 2.5. The larger gradients in the field lead to a reduced vertical and radial extent of the breakdown region, and a reduction in the maximum in the breakdown criteria. In figure 5e, the calculation for I_{OH} precharge of 20kA is repeated with a larger loop voltage and reduced non-axisymmetric fields for comparison to case shown in figure 5c. The predicted requirement for approximately 30% larger loop voltage between the 8 kA and 20 kA I_{OH} precharge scenarios was observed on NSTX-U where the requirement for larger loop voltage (4V) is close to the experimentally realized value (3.9 V).

One relative metric for comparison between the calculations is the average of the breakdown parameter (which is proportional to the field-line connection length) along a vertical segment between Z = -0.8 m to Z = + 0.8 m (figure 6). This reflects that the average axisymmetric flux contours in the time and spatial range of interest are mostly vertical due to the finite time-averaged vertical field. Thus, the vertical average of the breakdown parameter is roughly proportional to electric field available to accelerate electrons integrated along the spiraling field lines. The separate colors in figure 6 correspond to the calculations described in figure 5. The difference in this parameter between case B (blue) and case D (green) reflects the reduction in the poloidal field null size as the solenoid precharge value increases. Case C (orange) and case E (red) illustrate that the maximum in the vertical average value is similar to the NSTX case (black) with reduced non-axisymmetric fields and with a larger V_{loop} for the higher solenoid precharge case.

These calculations enabled rapid progress in producing the first discharges on NSTX-U by providing the needed guidance on the target I_{PF5} and the relationship between I_{PF3} and the choice of I_{OH} precharge and V_{loop}. The first plasma demonstration required eleven discharge attempts with steady progress toward the demonstration of a 20 ms discharge with a maximum I_p of 109 kA at a toroidal field of 0.5 T. The calculations also provided guidance on the changes to I_{PF3} and I_{OH} required when varying the I_{OH} precharge. Figure 7 shows two inner-wall limited discharges produced soon after the first boronization. One discharge has I_{OH} precharge of 8 kA (black lines) while the other discharge has an I_{OH} precharge near 20 kA (red lines). The requirement of about one additional loop volt (figure 7c) at increased I_{OH} precharge is consistent with the calculations for the two precharge levels. The difference in I_{PF3} between the two discharges (figure 7d) reflects the increased field required to null the fringe field from the central solenoid. I_{OH} and I_{PF3} currents are ramped toward negative current prior to t = 0 in order to apply a positive loop voltage. The change in solenoid flux is the primary driver of the V_{loop} needed for breakdown (2 – 5 volts is

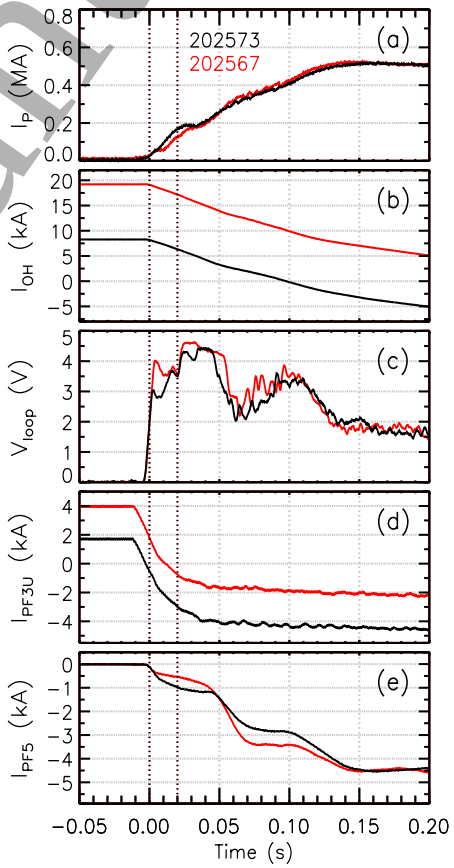

Fig 7 (a) Plasma current, (b) solenoid current, (c) loop voltage at the inboard midplane, (d) current in the upper PF3 coil and (e) the PF5 coils for two discharges that begin at different I_{OH} pre-charge levels. Vertical lines indicate the breakdown period from 0 – 20 ms.

typical), however the changing I_{PF3} current increases the loop voltage in the breakdown region by 0.5 V. The coils near the outboard midplane (I_{PF5}) are energized (negative current) after t = 0 in order to contribute to the confining vertical field for the newly formed current channel. Both discharges are inner wall limited using only the PF5 and PF3 coils to maintain a vertically and radially stable discharge (PF3U and PF3L currents are nominally matched). Feedback on I_p and the plasma position begins at t = + 20 ms, and soon after this transition the discharge evolution is similar indicating the choice of the ohmic precharge does not have a significant impact on the details of the discharge

At present, the vacuum field calculations are in good qualitative agreement with the experiment, however the model does not accurately predict the timing of the null formation (a difference of a few milliseconds) and the vertical position of the plasma following breakdown. This disagreement is under investigation, and may require including 3D effects, further refinement of the conducting structure model or including the vertical expansion of the ohmic solenoid that scales with I_{OH}. Nevertheless, the model was successful for identifying suitable starting conditions for achieving first plasma and developing a recipe for scanning parameters when optimizing the startup scenario.

5. Plasma control and error field correction enabling long pulse L-mode discharges

Low confinement (L-mode) discharges are typically utilized in tokamak research to enable scientific studies in a simplified plasma state that is highly reproducible. These qualities also make L-mode scenarios valuable for commissioning new systems that benefit from reproducible plasma conditions. Long-pulse L-mode discharges were quickly established on NSTX-U, enabling progress on commissioning tasks and providing a scenario for the first experiments.

5.1 Fiducial L-mode discharge

The longest beam-heated L-mode discharges on NSTX maintained I_p = 0.6 MA for 0.4 s; the length of these discharges was limited by the available Volt-seconds (V-s) of the ohmic solenoid. The increased diameter of the central solenoid on NSTX-U increases the available V-s by a factor of three, permitting longer L-mode discharges that achieve a relaxed current profile. During the commissioning phase, L-mode discharges with a flattop ending after 2 s were demonstrated with I_p = 0.65 MA, exceeding the length of the longest NSTX H-mode discharges [13].

A fiducial L-mode discharge was produced at the start of most run days during the final weeks of the commissioning period in order to evaluate the readiness of systems for operations and to provide a standard discharge to evaluate the evolution of wall

conditions. An example fiducial L-mode discharge is summarized in figure 8, where the plasma current (I_p) has a flattop at 0.65 MA for a duration exceeding one second with 0.6 T vacuum toroidal magnetic field at R = 1 m (figure 8a). The discharge is heated with 1 MW of NBI heating from beamline 1B and has regular sawteeth after 0.5s as observed in the oscillations in the neutron emission rate (figure 8b). Both the internal inductance (l_i) and β_N are approximately 1.3 during the period with regular sawteeth (figure 8c).

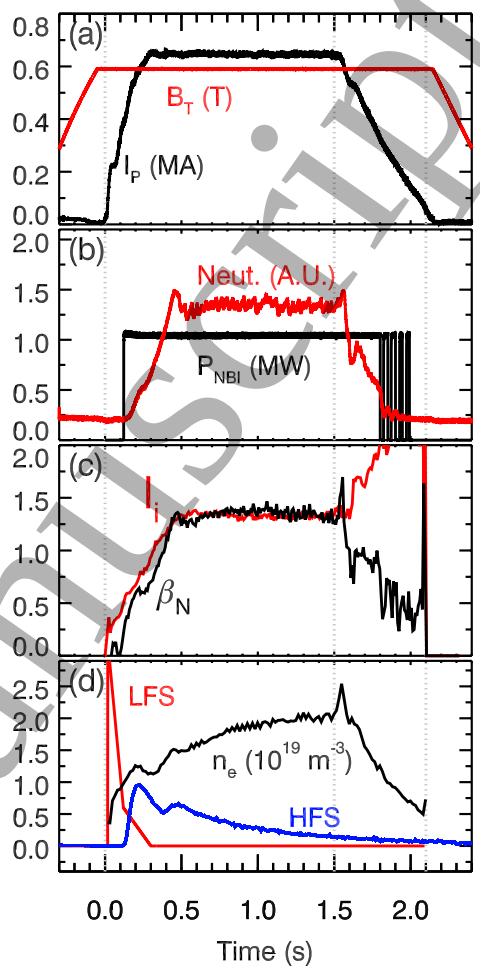

Fig 8 Example of a fiducial L-mode discharge (204179) with steady conditions for about one second.

Figure 8d summarizes the gas fueling sources and the resulting line-averaged density as measured by integrating the n_e profile measured by Thomson Scattering at the device midplane. The gas fueling is programmed prior to the discharge (i.e. feed forward control). About 10 ms after plasma breakdown, a piezo-electric gas valve on the low-field side (LFS) midplane is used to inject deuterium gas. The red trace in figure 8d is the requested flow rate in Torr-liters/second divided by 25 (max requested flow rate is 70 Torr l/s). The piezo-electric valve modulates between open and closed (order 100 Hz) to obtain an average flow-rate that matches the request. The modulation pattern is computed by the Plasma Control System (PCS) based on the requested flow rate and the starting pressure in the fueling plenum. The LFS valve is approximately 10 – 20 cm away from the plasma boundary and thus provides a diffuse injection to the outboard edge. The fueling rate needed to maintain the density through the flattop phase is reduced as the neutral pumping speed of the graphite tiles decreases [44].

The largest impact on the discharge density (black line) during the ramp-up phase is the deuterium fueling provided from a pair of puff valves on the high-field side (HFS) of the plasma These valves are opened at a prescribed time during the discharge and inject all of the gas stored in a plenum into long tubes that run behind the tiles of the center column and terminate at the injection orifice near the plasma boundary. There are two injectors near the midplane and two additional injectors near the upper shoulder of the centerstack. Within each pair, there is an injector with a ¼" diameter tubing and an

injector with an 1/8" diameter tubing. The ¼" diameter injectors are new to NSTX-U and provide a tool for injecting a shorter pulse of gas compared to the 1/8" diameter injectors due to the increased conductance with larger diameter tubes. The blue line in figure 8d shows the cumulative flow rate in Torr l/s from the two valves divided by 25. At 100ms, the ¼" diameter valve at the midplane injects neutral deuterium, followed by the 1/8" diameter valve at the midplane at 380ms. H-mode discharges used a similar neutral fueling scheme, except that the fueling provided by the first HFS puff was reduced by about a factor of two and the second HFS injection using the 1/8" diameter valve was not used.

The electron temperature (T_e) and density (n_e) measured by Thomson scattering during the flattop phase of discharge 204179 is shown in figure 9. The red and orange traces are the profiles before and after a sawtooth crash near the start of flattop, while the blue and black traces show similar profiles near the end of flattop. The vertical lines in figure 9 show the approximate location of the inversion radius of T_e during the crash. Each sawtooth crash significantly perturbs T_e, however the impact on n_e is modest, indicative of a large redistribution of high-energy particles. The density is slowly rising in the flattop phase, resulting in T_e at the inversion radius to decrease slightly.

Figure 10 compares the computed equilibrium plasma shapes at 0.7 and 1.5 seconds, demonstrating that the shape of the plasma boundary is well controlled. The fiducial L-mode discharge is biased downwards (in the direction of the ion grad-B drift) to produce a lower single null (LSN) shape with the outer strikepoint on the outboard divertor plate. The radial separation of the flux surfaces connecting the upper and lower X-points as measured at the outboard midplane (i.e. d_{rsep}) is about -0.5 cm where the

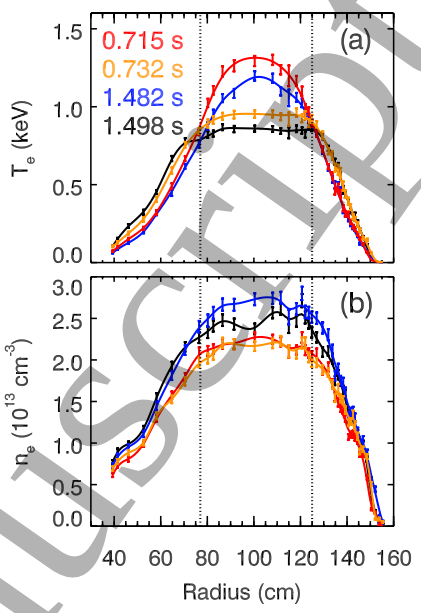

Fig 9 Electron temperature (a) and density (b) before (red, blue) and after (orange, black) a sawtooth crash at the beginning and end of flattop for discharge 204179.

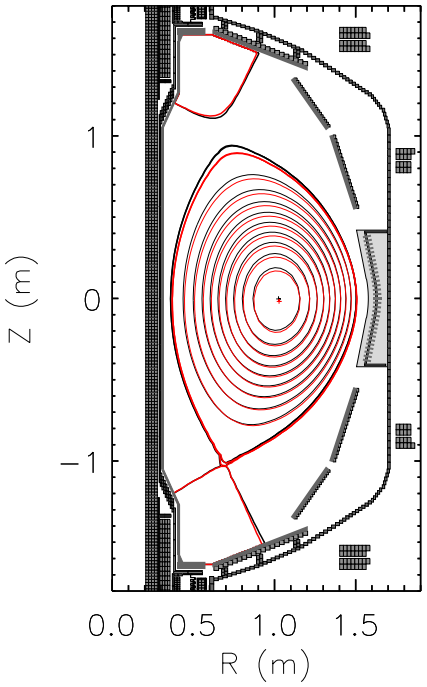

Fig 10 Magnetic equilibria for the fiducial L-mode discharge (204179) at 0.7s (black) and 1.5s (red).

negative sign indicates a LSN shape. The active control of the plasma shape through each phase of the discharge is described in the next section.

5.2 Plasma Current and axisymmetric shape control

The Plasma Control System (PCS) on NSTX-U was reorganized into a state machine control architecture, where the control algorithms that process realtime measurements and generate commands for the actuators are defined for each phase of the discharge. Figure 11 shows the five states defined in the PCS during commissioning operations and the possible paths through the various states. All discharges begin in the "Ramp-up and Flat-top" state (SS = 0) and end in either the SS = 3 or SS = 4 states.

In the fiducial L-mode discharge shown in figure 8, there are transitions to the "Slow I_p rampdown" state (SS = 1) at 1.5 s and the "Insufficient I_p" state (SS = 4) at 2.1 s (indicated by vertical dotted lines in figure 8). The "Slow I_p Rampdown" state attempts to reduce I_p and heating power while transitioning from a diverted to limited shape. In the case of the fiducial discharge, the switch to Slow I_p Rampdown is requested to occur at a defined time, but this state transition is also triggered in real-time if the ohmic solenoid current is approaching a current or heating limit.

The most common exit from the Ramp-Up and Flattop State in commissioning operations was via the Fast I_p Rampdown (SS = 2). This state is intended to avoid a disruption by rapidly reducing the plasma current, heating and elongation, and ending the discharge. Operations on NSTX-U entered the Fast I_p Rampdown state in response to the vertical excursions ($Z \bullet dZ/dt$ [45]) or the I_p fractional error $(I_{p,request} - I_{p,measure})/I_{p,measure}$ exceeding prescribed limits. The two terminal states in the State Machine are "I_{OH} Loss of Control" (SS = 3) and "Insufficient I_p" (SS = 4). The goal of these states is to return all of the coil currents to zero at the end of a discharge with no active feedback on the plasma properties. The "I_{OH} Loss of Control" state is entered when the ohmic solenoid current is projected to exceed its maximum current (– 20 kA in commissioning operations) within 5 ms. The "Insufficient I_p" state is entered when I_p falls below 100 kA; this is the terminal state for the fiducial discharge shown in figure 8.

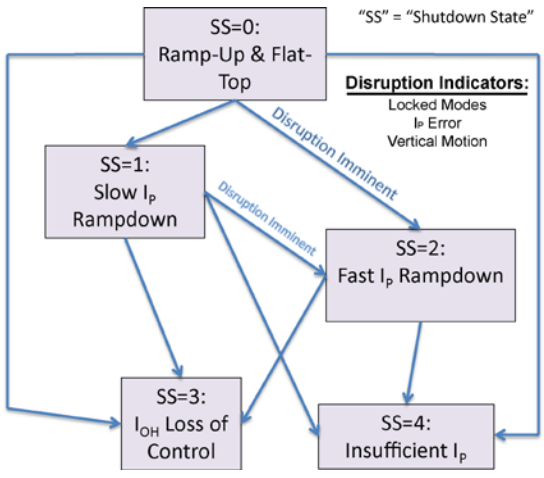

Fig 11 State machine transitions in the PCS control scheme.

A subset of the coil currents during the L-mode fiducial discharge are shown in figure 12 in order to describe the shape control algorithms during the different phases of the discharge. The ohmic solenoid (figure 12a), PF3U, PF3L and PF5 coil currents (figure 12b where I_{PF3L} is not shown but is similar to I_{PF3U}) are pre-programmed up until 20 ms into the discharge as described in Section 4. The currents are tailored for achieving breakdown at t = 0 and keeping the plasma vertically centered in the vessel as I_p increases to about 150 kA. At 20 ms (vertical blue lines in panels 12a – c), the feedback algorithm used to define the ohmic solenoid voltage transitions to a PI (i.e. proportional and integral) feedback algorithm based on a target I_p. Also at this time, the voltage control of the PF3U, PF3L and PF5 coils transitions to PI feedback algorithms based on the estimated radial and Z position of the outer boundary of the plasma. The radial position of the outer boundary is represented as two "gaps" (i.e. the average distance) from the primary and secondary passive plates, while the Z position is the up-down shift of the plasma outer boundary relative to the device midplane. The gap control algorithm generates voltage requests for the PF3 and PF5 coils, while the Z control algorithm generates an additional voltage request for the two PF3 coils. The gap voltage request for

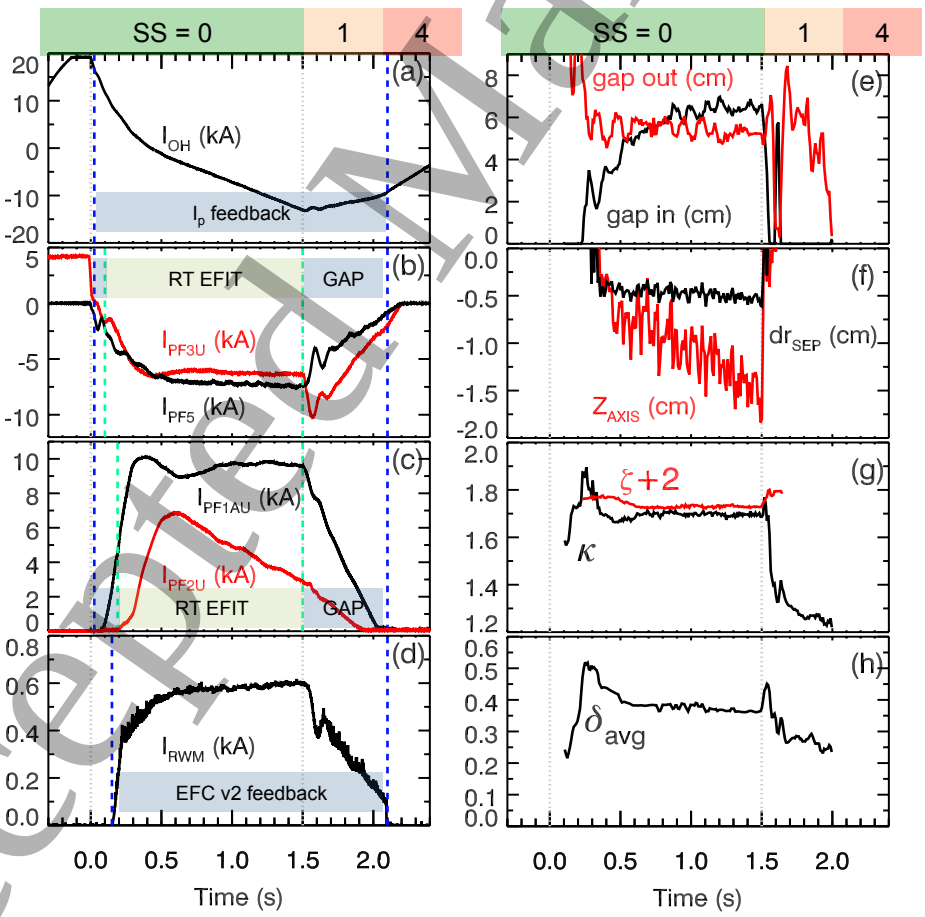

Fig 12 Waveforms for fiducial L-mode discharge (204179). Description of the coil currents (a – d) and plasma shaping parameters (e – h) is given in text.

the PF3 coils has the same polarity for the two coils, while the sign for the Z position voltage request is different for the two coils. The control of the voltage on the PF3 and PF5 coils transitions from gap and Z control to ISOFLUX [46, 47] shape control based on real-time EFIT (rtEFIT) [48,49] at 140 ms (vertical green line in figure 12b) when $I_p \approx$ 300 kA at 100 ms. Further details on the NSTX-U shape control algorithms can be found in [47].

A differential voltage proportional to small vertical motions (dZ/dt) is added to the voltage request for the PF3 coils derived from either shape control algorithm (gap or ISOFLUX) in order to maintain vertical stability. The vertical control algorithm used for most of the commissioning operations on NSTX-U had a number of advantageous changes compared to NSTX. One significant change was that the measurement of vertical motion used a weighted set nine sensor pairs instead of a single pair, as was done on NSTX [50]. Another significant change was the addition of signal conditioning that improved the signal-to-noise ratio of the vertical motion measurement. These improvements allowed NSTX-U to achieve similar levels of elongation at matched values of l_i compared to NSTX, despite operating at a larger aspect ratio.

The fiducial L-mode discharge had nearly up-down symmetric X-point positions, thus the current in each pair of upper and lower divertor coils is very similar. Figure 12c shows the current for the upper divertor coils where $I_{PF1AU} \sim I_{PF1AL}$ and $I_{PF2U} \sim I_{PF2L}$. The current in the PF1A coils is controlled at the beginning of the discharge using a relational algorithm with the current request equal to $I_{PF} = A\, I_P + B\, I_{OH} + I_{off}$ where I_p is the plasma current, I_{OH} is the ohmic solenoid current and I_{off} is an offset current request. The relational coefficients (A and B) can vary versus time and are chosen *a priori* from free-boundary calculations such that X-point position is fixed over a range of I_p and I_{OH} for a target plasma equilibrium. The relational control of the divertor coils is part of the gap control algorithm within the PCS, thus this phase is labeled as gap in figure 12c. ISOFLUX control of the divertor coils begins at 190 ms (vertical green line in figure 12c) near the time the discharge begins to divert. This control scheme alters the current in the PF1A and PF2 coils to achieve a target X-point position as computed by rtEFIT.

The discharge summarized in figure 12 first diverts around 0.2s. After that, the X-point position both increases in radius and moves vertically toward the midplane until 0.5s, reducing the triangularity and elongation. The PF coil currents become more negative to account for the change in the solenoid fringe field as I_{OH} ramps during the flattop phase (t > 350ms). This effect is especially large for the PF2 coil current (figure 12c) since the poloidal field produced by this coil set is well aligned with the OH fringe field.

The shape of the discharge is well controlled by the ISOFLUX control algorithm during the flattop phase (after 0.5s) as illustrated by shape quantities (figure 12e-h). There are seven PF coil actuators used for active feedback on seven shape parameters. The red traces in figure 12e-g show three parameters of the shape that are under active PID feedback control using the three outboard PF coils in the ISOFLUX algorithm: the outer gap (via PF5), d_{rsep} (via PF3s) and the average outer squareness plotted with an offset (via PF3s). The four quantities under active feedback control using the four divertor PF coils (PF1As and PF2s) are the R and Z of the two X-points.

One consequence of maintaining a non-zero d_{rsep} is the Z position of the magnetic axis (figure 12f) drifts slightly downward as the ohmic flux changes. This is due to the fact that the flux expansion near the secondary X-point decreases as the ohmic solenoid current becomes more negative. This alters the projection of the flux surface connecting the upper X-point and the control position at the midplane resulting in a downward shift of the plasma boundary in order to maintain a constant non-zero d_{rsep}. This motion also leads to an increase in the inner gap, which is not under active control for this discharge. The small decrease in both the plasma height and width conspire to keep the elongation (κ) nearly constant during the flattop phase, whereas the increase in the inner gap leads to a small decrease in the average triangularity during the flattop (figure 12h).

The "Slow Rampdown" state is initiated at 1.5s, changing the control algorithms used for shape control (vertical green lines at 1.5s in figures 12b-c). Control of the PF3 and PF5 coils returns to gap and Z control targeting a low elongation plasma shape that is limited on the center column. The algorithm for the divertor coil currents in the "Slow Rampdown" state decreases the current from the values at 1.5s to zero about 0.5s later. The algorithm for controlling I_{OH} in this state reduces the target I_p by a specified rate (1.2 MA/s). At 2.1s, the PCS state changes to "Insufficient I_p" and the OH solenoid and all PF coils are steadily ramped to zero current. This ramp-down sequence terminates the discharge while avoiding a vertical disruption event (VDE).

5.3 Error field correction

Error field correction (EFC) experiments completed during the commissioning phase focused on identifying the optimum toroidal phase and amplitude of an applied n=1 magnetic field from six windowpane coils that are close fitting to the outside of the vacuum vessel at the outboard midplane. The optimum n=1 EFC in NSTX-U was identified in three scenarios: (1) during the flattop of ohmic discharges; (2) during the flattop of 1 MW beam-heated L-mode discharges; and (3) during the early-time current ramp of both L- and H-mode discharges. These experiments established that the optimum n=1 field was strongly dependent on the plasma equilibrium, meaning that the optimum

phase or amplitude would change from scenario to scenario or even as a function of time within a single discharge [51].

The first EFC experiments were conducted during the flattop of an ohmic discharge. The amplitude of the applied n=1 correction was set to be proportional to the PF5 coil current (the main vertical field), which was anticipated to be the largest error field source in the machine [52, 53]. By changing the phase and relative amplitude of the applied n=1 correction over a series of discharges, the phase and amplitude that minimized the ohmic flux consumption and maximized the discharge duration were identified. This ohmic EFC prescription is henceforth identified as version one, or EFC v1.

In the beam-heated L-mode flattop experiments, a technique know as a compass scan was used to determine the optimum n=1 correction [54, 55,42] and was found to have the same amplitude but a different phase (by 55°) than in the ohmic experiments. This second EFC prescription, which is henceforth identified as version two, or EFC v2, was the first indication that optimum n=1 correction may be dependent on the plasma scenario. The fiducial L-mode discharge presented in this section uses EFC v2 with the amplitude of the applied n=1 field proportional to the PF5 coil current. Figure 12d shows the current in one of the six windowpane (RWM) coils around the midplane of NSTX-U. The proportionality factor relating the RWM coil current to the PF5 coil increases from zero to a finite value between 150 and 220 ms; the factor is unchanged after this time, including during the "Slow I_p ramp-down" phase (after 1.5s). Using either version of EFC directly enabled stable, long-pulse L-mode discharges.

A final set of preliminary EFC experiments focused on identifying the optimum EFC in the ramp-up phase of L- and H-mode discharges. These experiments found that the optimum early-time n=1 correction phase was opposite to that of the phase in EFC v2. In other words, the best phase of the n=1 EFC during the flattop of the discharge actually contributed to the error-field during ramp-up. In addition, the optimum correction in the L-mode ramp-up was found to be independent of the ohmic solenoid current, suggesting that the time-varying EFC was not due to the time-varying forces on the coils and vacuum structure as the ohmic solenoid current changes. These early-time EFC results provided further evidence of the equilibrium-dependent nature of the optimum n=1 EFC in NSTX-U.

Each effort to improve the n=1 EFC resulted in improved performance in L- and H-mode discharges. However, an equilibrium-dependent optimum n=1 EFC presented an operational challenge, thus a substantial effort is underway to identify and mitigate the source of the error field prior to resuming NSTX-U operations. Detailed spatial

metrology of key machine components following operations revealed that the center column of NSTX-U, which contains both the toroidal field and ohmic coils, was misaligned during installation. Using the metrology results in the IPEC [56] and M3D-C1 codes [57] has indicated that the misalignment of the center column, rather than the PF5 coils, was the primary source of the n=1 error fields during the commissioning operations. The modeling results show that error fields from the misaligned center column are introduced on the high field side of the plasma and lead to a difficult-to-correct equilibrium-dependent plasma response, consistent with the experimental observations [51]. Consequently, the process for aligning the center column is being updated to ensure stricter tolerances are enforced in order to reduce the magnitude of this error field source.

5.4 Diverted L-mode operating space

Progress was made during the commissioning period to explore the operating space of the stationary L-mode discharges in support of planned experiments [58]. The technical and stability limits to the achievable plasma shapes and pulse lengths are more restrictive as the plasma current (I_p) and density (n_e) increase for fixed B_T. For example, the inductive flux consumption rate increases with I_p and n_e, resulting in shorter flattop periods. Another constraint is the force on the structural components of the device, which scales with I_p. The most restrictive force in the L-mode scenario is the vertical force on the divertor coils when the absolute value of the product of the divertor coil and ohmic solenoid currents is large near the end of a discharge. The low-elongation ($\kappa \leq 2$) required for vertical stability when $l_i > 1.0$ requires the divertor coils operate at large currents and restricts the achievable triangularity to a modest range, typically 0.25 – 0.45. The desire to reduce l_i in order to maximize the achievable κ favors utilizing the maximum P_{NBI} that does not induce an L-H transition.

Figure 13 summarizes five notable L-mode discharges from the campaign that began to probe the operational limits. All of the discharges had $B_{T0} \sim 0.6$ T and a LSN shape similar to the fiducial shape shown in figure 10. The longest discharges on NSTX-U ran the I_{TF} flattop and NBI heating until the 2 s pulse-length limit enforced for commissioning operations. Discharge 204082 (black traces) is an example of discharge that begins a controlled ramp down at 2s, with $I_p = 0.65$ MA and $P_{NBI} = 1$ MW at low density ($n_e < 2 \times 10^{19}$ m^{-3}). The absence of neutral beam heating and the decreasing toroidal field during the rampdown phase results in an MHD event that triggers the PCS to execute a fast rampdown.

L-mode discharges were run at higher densities by actively fueling throughout the discharge. These discharges ended prior to 2 s due to the ohmic solenoid current

approaching its limit. The I_p flattop in discharge 203577 (blue traces) ends at 1.73 s when the ohmic solenoid current reaches – 19 kA, triggering the PCS state to change to "Slow I_p rampdown." During this phase, the ohmic solenoid current reaches – 20 kA, which triggers the PCS state to switch to "I_{OH} Loss of Control," leading to a fast termination of the discharge during the rampdown. The larger n_e compared to 204082 (black traces) was required to avoid the L-H transition as the neutral beam absorption improved at larger I_p.

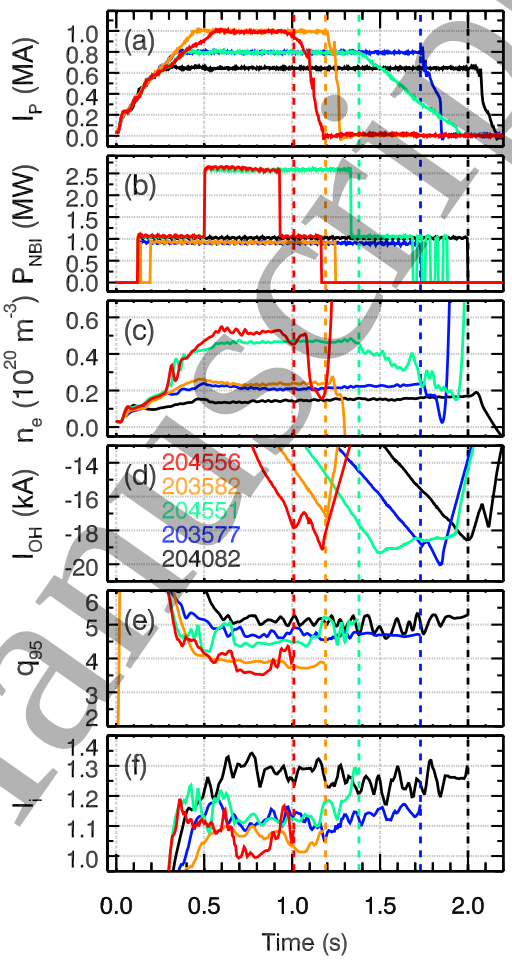

Fig 13 (a) Plasma current, (b) NBI heating power, (c) line-averaged density, (d) Ohmic solenoid current, (e) edge safety factor, and (f) internal inductance for L-mode discharges on NSTX-U

Many experiments benefit from running with P_{NBI} > 2 MW in order to collect ion measurements from the CHERS diagnostic. Thus, a series of L-mode discharges were run with higher density in order to remain in L-mode while injecting P_{NBI} = 2.5 MW. Discharge 204551 (green traces) is an example of an L-mode discharge at larger density and heating power. The ohmic current threshold for switching to the "Slow I_p rampdown" state was set to – 18 kA for this discharge to maintain I_{OH} > - 20 kA during the rampdown phase. Despite the increase heating power, the larger fueling rates required for the elevated density results in a lower T_e and an increased ohmic flux consumption rate and, thus, a shorter discharge compared to 203577 (blue trace).

L-mode discharges up to I_p = 1 MA were achieved at B_{T0} = 0.6 T and are stable with q_{95} = 3.7. No L-mode discharges were attempted with I_p > 1 MA, thus the I_p / B_T limit imposed by MHD stability was not established. The I_p flattop ends in 203582 at 1.2 s when I_{OH} is – 17.5 kA due to exceeding the conservative force limit threshold on the PF1A coil as calculated by the Digital Coil Protection System (DCPS). Discharge 204556 (red traces) operates at I_p = 1 MA but I_{OH} achieves – 19 kA without triggering a DCPS warning by requesting a lower triangularity shape, resulting in more current in PF2 and less in PF1A in order to keep all divertor coil forces within limits. Discharge 204556

(red traces) is another example of a discharge run at higher n_e and larger P_{NBI}; the early termination of one of the beams leads to the rapid appearance of 3/2 tearing mode about 50 ms prior to the switch to "Slow I_p rampdown" at 1.0 s when $I_{OH} = -18$ kA. The MHD activity during the controlled rampdown results in the PCS switching to "Fast I_p Rampdown" around 1.1s.

L-mode discharges on NSTX typically achieved flattop time of less than 0.4 s for $I_p \sim 0.7$ MA and did not achieve a relaxed current profile. Thus, the realization of both longer and higher I_p L-mode scenarios on NSTX-U provides a significant increase in the ability to characterize L-mode transport in a low-A geometry for comparison to standard aspect ratio devices [58]. Future operations will aim to characterize the operational and stability limits to I_p, q_{95}, shaping parameters and density in diverted L-mode discharges on NSTX-U. Preliminary calculations indicate that diverted L-mode shapes at $I_p = 1.6$ MA, $B_T = 1$ T and $q_{95} = 4$ can be realized within the DCPS limits chosen for the commissioning phase provided $\kappa \geq 2$. The minimum elongation is dictated by the current limit on the divertor coils required to operate within the force limit thresholds on the PF coils when the ohmic solenoid is at large negative current. A stable elongation greater than 2 was achievable during the first NSTX-U campaign provided $l_i \leq 1.05$. As shown in figure 13f, the l_i in L-mode discharges approached $l_i = 1.05$ at $I_p = 1$ MA and $q_{95} = 4$, suggesting the elongation could have been expanded to $\kappa \geq 2$. Perhaps the more restrictive challenge to realizing L-modes at $I_p \geq 1.2$ MA is the limit to the pulse length due to the increased rate of flux consumption at higher I_p. Thus, future operations will work to minimize the flux consumption of the I_p ramp-up scenario for L-mode discharges [59] and characterize the dependence of the flux consumption on B_T toward enabling L-mode operations at plasma currents above 1.2 MA.

6. High-performance H-mode operation

One goal for the commissioning period was to establish a reproducible H-mode scenario that had regular ELMs and little core MHD activity to facilitate future scientific operations. Figures 14, 15 and 16 compare a representative H-mode fiducial discharge on NSTX with large ELMs (green traces) and three H-mode discharges from NSTX-U (blue, red and black traces) chosen to illustrate the progress toward achieving the commissioning goal. Figure 14 compares the boundary shapes at t = 0.6 s for the discharges of interest. The increased major radius of the inboard limiter results in an increase in the discharge aspect ratio from 1.4 to 1.6 – 1.7. The NSTX discharge had $B_{T0} = 0.45$ T, while the NSTX-U discharges had $B_{T0} = 0.6 – 0.63$ T. Another difference is the NSTX reference discharge was produced with lithium wall coatings, whereas the NSTX-U discharges are produced with boronized walls. The vertical dashed lines in figures 15 and 16 designate the L-H and H-L transitions for each discharge.

The NSTX discharge (green traces) uses close to the maximum available heating from the three neutral beams (figure 15b). The available NBI heating power increased from 3 MW up to 10 MW throughout NSTX-U commissioning operations as the six neutral beam lines were conditioned. In the third week of operations (blue traces), 3 MW of heating was available with 2 MW coming from the original beam lines (1B and 1C) and 1 MW from the most on-axis beam line of the new NBI system (2C). The cumulative heating power increased to 4 MW by the fifth week (red traces) with a total of 3 MW sourced from 1B and 1C and 1 MW sourced from the most off-axis beam of the second beam line (2A). About 5.5 MW of beam power was achieved in the seventh week (black traces) with the addition of 1.3 MW from beamline 2C and an increase in the heating power of 2A (1.2 MW) compared to fifth week. All six beamlines were conditioned to at least 80 keV by the ninth week, providing the capability to inject up to 10 MW, however no discharges were attempted with $P_{NBI} > 6$ MW.

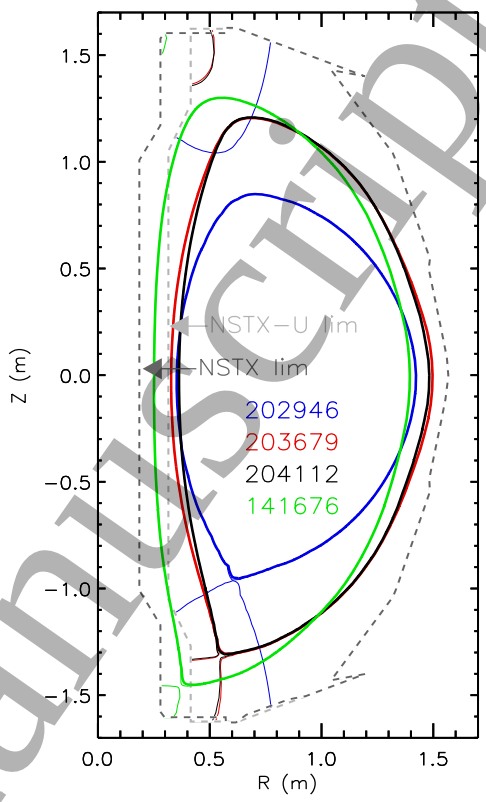

Fig 14 Equilibrium boundary at 0.6 s for three NSTX-U H-mode discharges (blue, red and black) compared to an NSTX H-mode discharge (green).

6.1 First H-mode discharges on NSTX-U

H-mode was first obtained on NSTX-U during the second week of the campaign. The blue traces in figure 15 are data from a typical H-mode discharge achieved during the third week. The L-H transition occurs soon after the start of the I_p flattop (figure 15a) with 3 MW of neutral beam heating (figure 15b) when the internal inductance (l_i) is above 1 (figure 15c). The internal inductance sustained during H-mode ($l_i \sim 0.9$) restricted the maximum elongation ($\kappa < 1.8$) to values typical of diverted L-mode discharges. Furthermore, these discharges were produced prior to implementing improvements in the vertical stability control and correcting for error fields, which further limited the maximum elongation and plasma current. The small elongation constrained the outer strike point to be on the outer divertor plate, similar to diverted L-mode discharges (figure 14).

Following the L-H transition, the global density (figure 15e), stored energy (figure 15f), β_N (figure 15g) and global energy confinement time (figure 14h) rise during an ELM-free period. The D_α emission from the lower divertor (figure 16a) shows three small ELMs between 0.5 and 0.6s. MHD activity (figure 16b) increases with the rise of β_N and a long-lived rotating n=1 mode appears 100 ms after the transition. These first H-mode discharges had few or no ELMs due to the heating power being close to the power required to remain in H-mode, thus the impurity content accumulated through the H-mode period as inferred from visible imaging and spectroscopy diagnostics. The resulting increase in radiated power, combined with the MHD induced transport, reduced

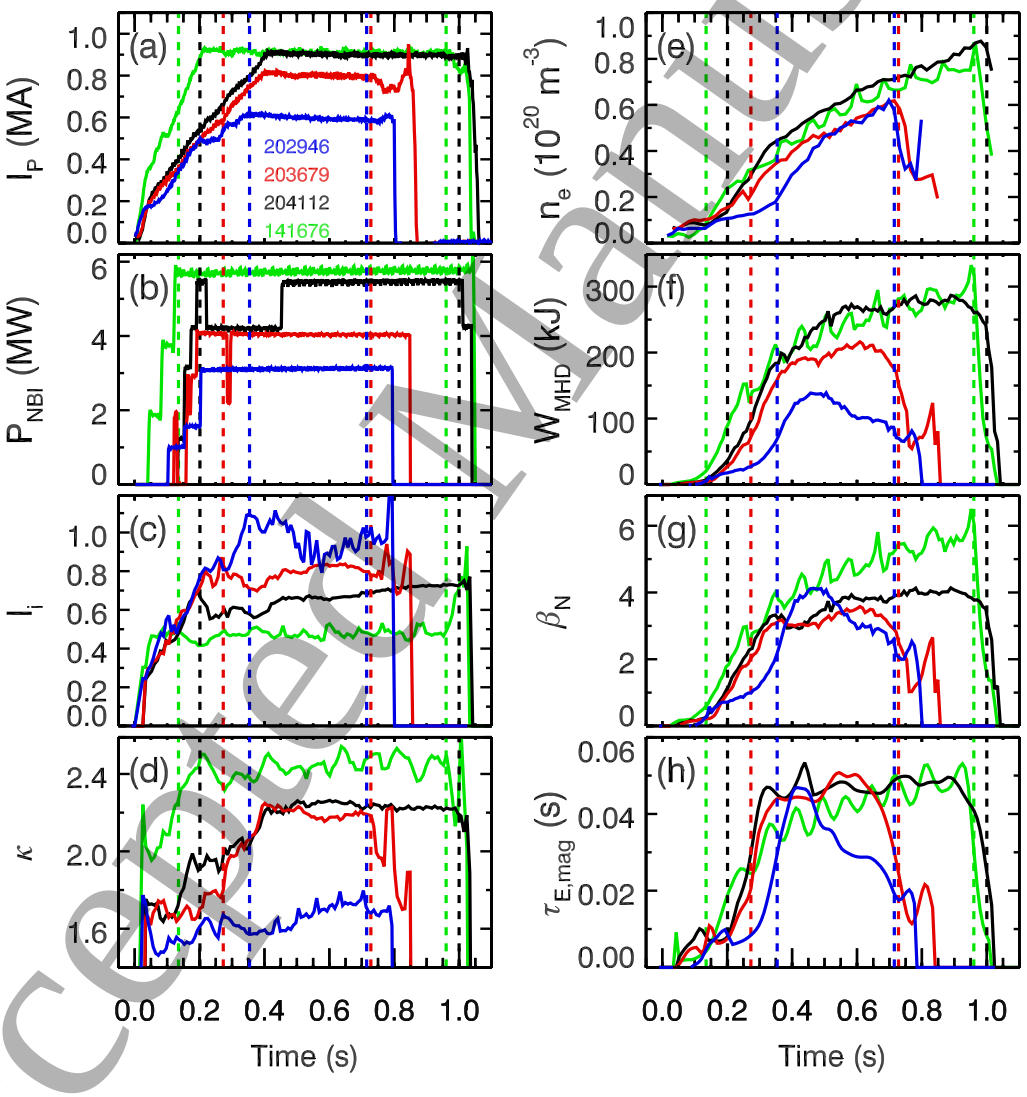

Fig 15 Three NSTX-U H-mode discharges (blue, red and black traces) compared to a fiducial NSTX H-mode discharge with large ELMs (green traces). Vertical lines show L-H and H-L timing. Description of the parameters provided in the text.

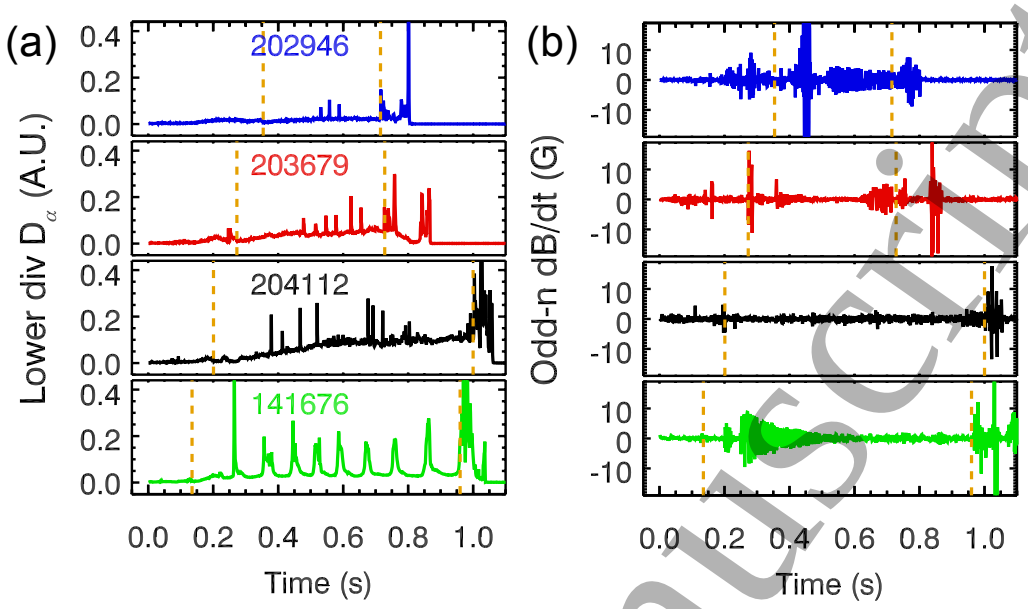

Fig 16 (a) D_α emission from the lower divertor and (b) low frequency odd-n magnetic perturbations at the outboard midplane for the four discharges shown in figure 15.

the stored energy and eventually drove the discharge to an H-L back transition due to insufficient heating power to sustain the H-mode state.

6.2 Operations at increased elongation

Triggering the L-H transition within the I_p ramp-up was shown to be a critical component for achieving high-performance discharges on NSTX. The increased edge temperatures and pressure gradients in H-mode act to reduce the penetration of the edge current that drives the increase in l_i during the ramp-up phase. Consequently, the rise in l_i is slowed after the L-H transition, increasing the achievable elongation and average triangularity (δ) in the flattop phase [60]. This is beneficial since the increased shaping acts to increase the I_p limit imposed by edge stability limits. Furthermore, the reduction in the pressure peaking in H-mode permits stable operation at higher β_N. At larger I_p, more heating power can be injected while remaining below global β_N limits, which is beneficial for inducing the regular ELMs needed to flush impurities from the plasma core and maintain operation at reduced l_i.

H-mode discharge development restarted in the fifth run week with the goal of increasing the elongation of the H-mode discharges by moving the L-H transition into the rampup phase and leveraging a number of new shape control capabilities. These capabilities included using rtEFIT and ISOFLUX to provide real-time control of the outboard boundary and the improvements in the active vertical stability control (multi-sensor detection and signal conditioning) described in section 5.2. The first version of

error field correction (described in section 5.3) was available, enabling MHD stable operations at higher β_N.

Progress on the development of a high-performance H-mode scenario in the fifth run week is shown by the red traces in figure 15, where the L-H transition occurs prior to 0.3s and l_i is below 0.8 for the entire discharge. The lower l_i combined with improvements in the vertical control system enables the realization of an elongation ($\kappa \sim 2.2$) comparable to NSTX at $l_i = 0.8$ despite the larger aspect ratio (see figure 3a in [13]). The discharge achieves the commissioning target with a period of routine ELMs with $\beta_N > 3$ and minimal core MHD activity from 0.45 – 0.6s (figures 15g and 16b). The increased elongation enables a high triangularity shape with the outer strike point terminating on the inner divertor (figure 14).

6.3 Operations with improved error field correction

H-mode operations in the seventh week of the commissioning period accessed $l_i \sim 0.7$ by moving the timing of the L-H transition before 250 ms. These discharges achieved larger ratios of β_N/l_i that made the discharges more at risk for MHD activity that could lead to a disruption. Measurements of the current profile from the Motional Stark Emission (MSE) diagnostic were not available during the commissioning phase, thus a rigorous analysis of the *q*-profile and stability properties of these discharges cannot be completed. However, the phenomenology of the discharges, combined with an estimate of q_{min} from partially-kinetic EFIT02 reconstructions (n_e and T_e contribute constraints on the equilibrium), suggests the stability properties are consistent with H-mode discharges on NSTX.

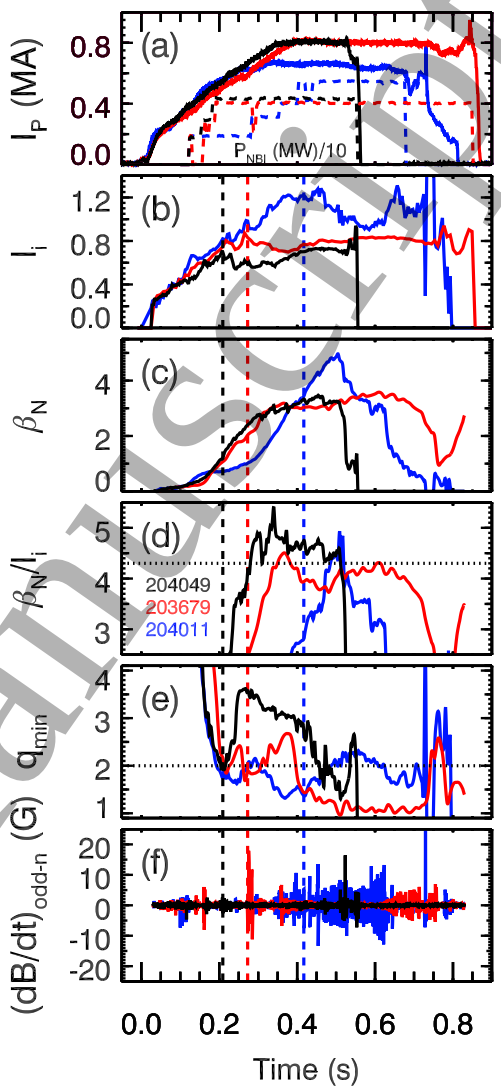

Fig 17 Comparison of three H-mode discharges that become MHD unstable. Plots are described within the text.

Figure 17 compares three H-mode discharges using the first version of EFC. The vertical lines in panels b-f show the timing of the L-H transition. Discharge 203679 (red

trace in this figure and figure 15) to a discharge 204049 (black traces) that has an earlier L-H transition and discharge 204011 (blue traces) that has a later L-H transition, near the start of flattop. The black and red traces are for discharges that have a similar LSN shape with $\kappa \sim 2.2$, heating and β_N. Figure 17a shows the plasma current (solid lines) and the neutral beam power in MW divided by 10 (dashed lines). The earlier L-H transition (near 0.2s for 204049) maintains a lower l_i (figure 17b) and, thus, a larger ratio of β_N/l_i through the flattop phase (figure 17d). The horizontal dotted line in figure 17d indicates an empirical stability limit of $\beta_N/l_i = 4.3$ when $q_{min} < 2$. Around 0.45s, the estimated q_{min} (figure 17e) goes below 2 for discharge 204049 (black) initiating MHD activity that leads to a disruption.

Discharges that approach the empirical β_N/l_i limit with q_{min} already below 2 tended to initiate MHD activity that reduced β_N and survive much longer before an H-L back transition leads to a disruption. Discharge 203679 (red traces) achieves a β_N/l_i ratio near the empirical limit with $q_{min} < 2$ at 0.6s and a slowly growing MHD mode begins. A corresponding H-mode experiment reproduced the $\beta_N/l_i = 4.3$ stability limit in a lower elongation shape at $l_i = 1.12$, $\beta_N = 4.8$ (blue traces); this was the largest β_N achieved on NSTX-U in the initial run campaign. Both 203679 (red) and 204011 (blue) are examples of discharges that approach the empirical β_N/l_i limit with $q_{min} < 2$ and have a long-lived MHD mode, while 204049 (black) is an example of a discharge that disrupts soon after q_{min} goes below 2 with $\beta_N/l_i > 4.3$.

Figure 18 shows a database of H-mode discharges on NSTX-U. Each data point is produced by a single EFIT02 calculation and only times with $q_{min} < 2$ are shown. The black points represent discharges completed with the first version of EFC. The blue line shows the empirical β_N/l_i limit of 4.3. Points above this threshold were achieved transiently as q_{min} decreased below two during flattop or an increase in the heating power increased β_N.

The early L-H transition discharges were repeated using an updated error-field correction algorithm (version 2 as described in section 5.3) resulting in a significant improvement in the stability of discharges with $\beta_N/l_i > 4.3$. This improvement is consistent with operations on NSTX that extended the range of stable β_N/l_i via a reduction in the n=1 error field [61]. The

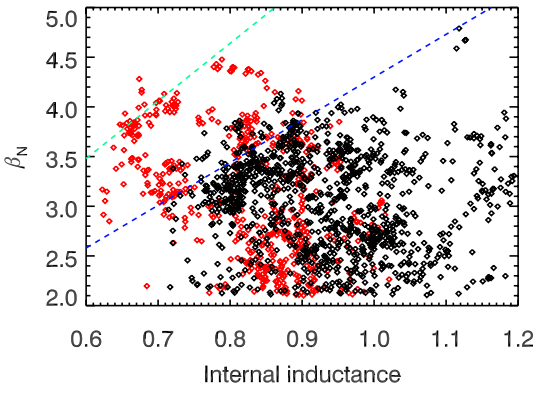

Fig 18 Database of equilibrium from H-mode discharges with $q_{min} < 2$ before (black) and after (red) changing to EFC version 2. Blue and green lines show $\beta_N/l_i = 4.3$ and 5.8, respectively.

maximum amount of heating power available in the seventh week of operations (5.2 MW) could be injected with stable operation near $\beta_N/l_i \sim 5.8$ (red points and green line in figure 18). The increase in the heating power between 204112 (figure 15 black trace) and 203679 (figure 15 red trace) was due to the addition of 1.2 MW at 0.45 s.

The early timing of the L-H transition in 204112 maintains l_i below 0.75 for the entire discharge (figure 15c). The elongation limit at this l_i was not explored, thus the achievable elongation is expected to be higher than what was demonstrated ($\kappa \sim 2.2$). The line-averaged density (figure 15d) rose steadily through the discharge and approached the Greenwald limit at the end of the H-mode period. The stored energy exceeds 250 kJ for about 0.4s corresponding to a $\beta_N \sim 4$. The ELM events are a mix of medium and small ELMs [62], with the smaller ELMs becoming more prevalent as the density and baseline D_α light increase. The discharge becomes ELM-free shortly after 0.9s suggesting the discharge heating is insufficient for triggering ELMs as the density rises. The ELMs are smaller and more frequent than NSTX discharges produced with lithium wall conditioning, such as 141676. This is consistent with previous NSTX experiments where small ELM regimes were accessed at higher collisionality and smaller triangularity [63].

One notable difference between discharges like 204112 (black traces) and the NSTX H-mode fiducial (green traces) is the relative absence of MHD activity around 0.3s (figure 16b). Future operations will investigate the role of the plasma current ramp rate, beam voltage, toroidal magnetic field and injection from the most tangential neutral beam lines on the nature of the early MHD activity near the start of flattop. This MHD activity was ubiquitous on NSTX, and it is encouraging that MHD quiescent H-mode scenarios on NSTX-U can be realized. Also, discharge 204112 achieves a similar volume averaged pressure to the NSTX reference, but the larger toroidal field leads to a comparatively smaller β_N. Calculations of the no-wall β_N limit for 204112 [64] indicate that this discharge operates at or slightly above this limit. Future operations will implement active RWM feedback to permit stable operation at larger values above the no-wall limit [15].

The thermal energy confinement computed using TRANSP is similar for 141676 and 204112 at 0.85 s ($\tau_{E,th} \sim 100$ ms) and is greater than the confinement derived from the ITER ELMy H-mode scaling for both discharges ($H_{98y,2} \sim 1.1 - 1.3$). The thermal energy confinement of 204112 is consistent with the OLSR version [65] of the NSTX confinement scaling derived using ELMing discharges with Boronized wall conditioning ($H_{ST06} \sim 1$) [13]. Future operations with an expanded suite of diagnostics and a larger range of discharge scenarios will improve the constraints available to quantify the thermal confinement in NSTX-U H-mode discharges over an expanded range of discharges parameters, particularly the electron collisionality, I_p and B_T. The non-

inductive current drive fraction in 204112 is computed using TRANSP to be about 35% with 0.05 MA of beam-driven current and 0.27 MA of bootstrap current at 0.85 s. The modest non-inductive current drive fraction is consistent with the impact of operating with an elongation below 2.5 and neutral beam voltages below 90 keV [5].

6.4 Advances toward improved H-mode discharge repeatability

The H-mode performance achieved during the seventh week of operations was difficult to reproduce in the final three weeks of operations. The primary challenge was that the H-mode scenario achieved the desired shape evolution using feed-forward divertor coil currents (see the "relational control algorithm" of the divertor coil currents discussed in section 5.3). This strategy requires a reproducible L-H transition timing and that the β_N and l_i match the target evolution in order for the pre-programmed divertor coil currents to be consistent with the desired shape evolution, particularly with the time of diverting and the formation of an inner gap. When using relational control of the divertor coils, the feed-forward neutral beam injection or the algorithm coefficients would be slightly modified between discharges (i.e. shot-to-shot) to keep the L-H timing within the target range and achieve the target β_N, l_i and shape evolution. This recipe was sufficient for operations where the wall conditions and NBI characteristics evolved slowly over the course of many discharges and are generally reproducible over the course of many days. However, this was often not case during commissioning operations, leading to difficulties achieving reliable H-mode performance using feed-forward divertor currents.

The H-mode discharges produced in the seventh week were the last H-mode operations following a full-boronization; operations in the last three weeks used nightly mini-boronizations with H-mode scenario development typically scheduled for the first discharges of each day. As discussed in Section 3, high-power H-mode discharges led to a rapid degradation of the wall conditions during H-mode operations, especially with mini-boronizations. Consequently, about ten to thirty discharges could be completed following a boronization before the oxygen content began to limit access to high-performance H-mode. Moreover, significant shot-to-shot differences in the wall-conditions increased the likelihood of missing the target L-H timing. Another complication during the commissioning period was that unplanned interruptions in operations and the concurrent conditioning of the neutral beams to higher voltage impacted the reliable injection of the neutral beams. Common issues included a delayed beam turn-on time and differences in the available power when repeating discharges. Furthermore, the mix of available neutral beams and voltages often changed, prompting a retuning of the rampup phase.

The challenges encountered in reproducing discharges using feed-forward divertor currents accelerated the development of H-mode discharges using ISOFLUX control of the divertor coil currents prior to the time of diverting, similar to the L-mode scenario described in section 5. This included the demonstration of X-point R and Z position control during the limited and diverted phase of the discharge, plus the inclusion of inner gap control with a multiple-in multiple-out (MIMO) control algorithm [47]. The MIMO algorithm controls the inner gap size by altering the target shape of the outer boundary and/or the X-point positions. This capability led to an improvement in the reliability of the diverting time and boundary evolution independent of the evolution of β_N and l_i, which depend on the details of the heating and wall conditions. An example is shown in Figure 19, where the time of diverting as well as in the X-point and inner gap width is reproducible despite two different levels of neutral beam power. The difference in P_{NBI} leads to different β_N, requiring a slight shift in the outer boundary and different levels of divertor coil currents in order to achieve the matched inner boundary. The activities related to improved shape control in H-mode were nearing completion at the end of the commissioning campaign and will be advanced via modeling prior to the start of the next operating period.

The inability to reliably reproduce the target H-mode scenarios during the final weeks of operations motivated the development of a database of diverted L- and H-mode discharges on NSTX-U with $P_{NBI} \geq 3$ MW in order to identify the target conditions for reliable H-mode access during ramp-up. H-mode was observed with heating power as low as $P_{NBI} = 0.9$ MW during the I_p flattop, however larger heating power is required to reliably trigger an H-mode transition at lower I_p. The database includes 68 L-H transition times and 100 times when the discharge was diverted but remained in L-mode or dithered (brief entry and exit into H-mode) during the I_p ramp-up phase. The database was used to identify a set of criteria that excluded most or all of the L-mode points from the database while keeping as many H-mode discharges as possible. Many of the criteria explored were motivated by observations made during the course of operations.

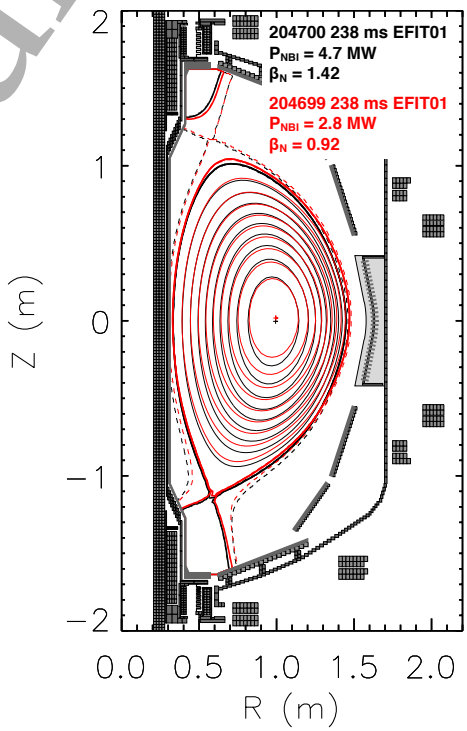

Fig 19 Comparison of two discharges with different heating power near the time of diverting. Slight changes to the requested outer boundary position made in real-time by the controller allow the X-point locations and inner gap width to be matched.

A set of four criteria was found to eliminate all L-mode points in the database. The first criteria is that the line-averaged density must exceed a minimum value ($n_e > 1.25 \times 10^{19}$ m^{-3}), the second criteria is that the surface voltage of the plasma must be sufficiently small ($V_{surf} < 1.15$), the third criteria is that the shape should be close to double null ($|dr_{sep} - 0.2$ cm$| < 0.6$ cm) and the fourth criteria is that the oxygen content of the plasma should be below a threshold (O II/ $D_\gamma < 0.1$). The offset of 0.2 from symmetry of dr_{sep} about zero (third criteria) may be attributed to systematic differences between the computed and realized equilibrium shape. The last criteria is a metric specific to NSTX-U, determined by taking the ratio of two filterscope measurements over a brief period near the beginning of a discharge and dividing by ten. This ratio is typically around 0.03 following a boronization and rose throughout a campaign as the walls deconditioned (see figure 3). Other limits to parameters such as I_p and dI_p/dt were considered, but did not result in a winnowing of the L-mode data points relative to the H-mode data points.

All 100 diverted L-mode time points chosen for the database are excluded by the criteria with two-thirds (67 entries) excluded by two or more of the criteria. About half (39 of the original 68) of the L-H transition entries satisfy all four criteria and most (63 out of 68) of the entries meet three of the four criteria. These results suggest it is unlikely to trigger an L-H transition with only two criteria met and very likely with all four provided $P_{NBI} \geq 3$ MW. These results informed the target the boundary shape, neutral fueling and loop voltage evolution when developing the rampup period of the H-mode scenario during the final week of operation. The ramp-up scenario was modified to have a pause in the I_p ramp in order to achieve $V_{surf} \sim 1$ V at the same time that the shape was diverted near balanced DN and $P_{NBI} > 3$ MW. The improvement in reliable triggering of the L-H transition with an I_p ramp pause and DN shape was also observed in NSTX [60]. Furthermore, the HFS fueling timing and magnitude was chosen to insure a density near 1.5×10^{19} m^{-3} and that a transient increase in V_{surf} near the time of maximum flow rate occurred before the target L-H transition time.

The changes to both the shape control and ramp-up scenario demonstrated improved reliable timing of the L-H transition and resiliency to variations in the wall conditions and heating evolution. Nevertheless, the best H-mode performance from the seventh week of operations was not replicated during the final three weeks of operations. The most likely cause was the switch from full- to mini-boronization strategies, although other operational challenges, such as changes to the neutral beams and shape control issues near the time of diverting also played a role. Modeling and analysis work is underway to aid in optimizing the ramp-up scenario to simultaneously provide access to low-l_i and low-flux consumption scenarios while improving the resiliency of the scenario

to variations in the wall conditions, heating and fueling in order to accelerate the realization of high-performance H-mode when operations resume on NSTX-U.

7. Summary and Future Plans

The initial ten weeks of operation on NSTX-U focused on commissioning activities that qualified the tools and scenarios required for the first experimental campaign. The scenario development activities comprised the majority of the commissioning activities and encompassed the demonstration of reliable plasma discharge startup at different levels of ohmic solenoid current precharge, development of long-pulse and high-current L-mode discharges that leveraged the larger field and ohmic flux of the center stack and producing ELM-ing MHD-quiescent H-mode discharges that met or exceeded NSTX performance at larger B_T.

The swift demonstration of the first 100 kA plasma discharge on NSTX-U was aided by calculations that established a process for adjusting the timing of the magnetic null and the applied loop voltage via changes to the evolution of the ohmic solenoid and poloidal field coil currents. The calculations also accelerated the development of startup scenarios over a range of ohmic solenoid precharge. Future work will aim to improve quantitative agreement between the calculations and experiment, and to minimize the flux consumption of the breakdown scenario for different levels of B_T in order to maximize the operating space of long-pulse L-mode discharges and to limit the rise in l_i via a larger I_p ramp rate.

The increased flux of the central solenoid extended the length of the L-mode discharges such that a number of L-mode discharges simultaneously exceeded the longest pulse duration and largest B_T demonstrated on NSTX. Discharges with 1 MW of neutral beam heating achieved a full relaxation of the current profile as evidenced by the occurrence of regular sawteeth. Active feedback of the plasma shape was demonstrated, first using feedback on the radial gaps between the outboard plasma boundary and the magnetic sensors, and then, by the third week of operations, using a real-time reconstruction of the plasma boundary. The long-pulse stationary L-mode discharges are novel for spherical tokamaks and enabled initial experiments in error field correction, transport and fast-ion physics. Initial experiments explored the operating constraints on these L-mode scenarios up to I_p = 1 MA and P_{NBI} = 3 MW. Future experiments will continue to quantify the engineering and physics limits to extending the L-mode scenarios to larger ranges of B_T, I_p and heating power. This includes the force and heating limits enacted in the real-time digital coil protection system and limits to the heating of the outboard divertor PFCs. Stationary L-mode discharges provide a valuable

scientific tool for validating plasma transport and stability models and can access moderate-β regimes that are comparable to conditions in standard aspect-ratio devices.

Error field correction (EFC) experiments were conducted in long-pulse ohmic and neutral beam heated L-mode discharges. Each effort to quantify the optimum EFC phase and amplitude of the n=1 EFC led to improved performance in L- and H-mode scenarios. The primary improvement in H-mode discharges was the realization of stable operation at increasing β_N/l_i and achieving $\beta_N/\beta_{N\text{-nowall}} \geq 1$. However, these experiments also identified that the optimum EFC was equilibrium-dependent, meaning the phase of the optimum EFC would change through the course of the discharge and was sensitive to the details of the scenario. Metrology of the device, coupled with calculations of the 3D plasma response, identified the misalignment of the inner TF leg as the primary source of the equilibrium-dependent error field. The inner TF leg will be realigned prior to the next experimental campaign in order to reduce the equilibrium-dependent error fields that are difficult to actively correct in experiments.

Many of the new hardware and software capabilities of the plasma control system (PCS) that were completed during the construction of NSTX-U were successfully deployed during commissioning operations. One new capability was the implementation of a state machine architecture that enables future development of active disruption avoidance. Preliminary work during the commissioning phase demonstrated the capabilities of the PCS to detect disruption precursors and initiate a rampdown sequence. A major research endeavor on NSTX-U is focused on the development of disruption detection, avoidance and mitigation strategies within the real-time system. The detection of the plasma vertical motion was improved by increasing the number of sensors used in the calculation and employing signal filtering that mitigated the impact of power supply switching noise. These advances allowed NSTX-U to achieve a similar elongation as NSTX for discharges with $l_i > 0.8$ despite the increased aspect ratio. Future operations will examine the maximum elongation for low l_i discharges ($l_i < 0.8$) in order to enable the large I_p and large non-inductive fraction scenarios that are predicted to be attainable at large elongation ($\kappa \geq 2.5$).

High-performance H-mode discharge development made steady progress through the commissioning period. The first H-mode discharges were produced during the second week of operations with 3 MW of neutral beam heating power. Steady progress toward the target H-mode performance with regular ELMs and minimal MHD activity was paced by improvements in the EFC, axisymmetric control and the available neutral beam heating. The target scenario utilizes an L-H transition during the I_p ramp-up phase to slow the current penetration and establish a high-elongation shape. The highest-performance H-mode discharges were produced in the seventh week of operations with I_p

≤ 1 MA at $B_T = 0.63$ T. These discharges had periods of regular ELMs and long periods of MHD-quiescence with good normalized energy confinement ($H_{98y,2} \sim 1.1$ and $H_{ST06} \sim 1$).

H-mode scenario development in the final three weeks of operations did not reproduce the performance achieved in the seventh week. The challenge in reproducing these results motivated the further development of shape control tools, such as the first demonstration of inner gap control without inboard PF coils. Analysis of the ramp up scenarios identified four criteria for achieving a reproducible L-H transition timing: exceeding a critical density, being close to a double null shape, maintaining a low surface loop voltage and having well-conditioned PFCs as measured by the oxygen content of the plasma. These findings motivated changes to the ramp-up scenario, such as the introduction of a pause in the I_p ramp to ensure a low surface voltage. Ongoing analysis and modeling efforts aim to identify control and scenario strategies that will accelerate the optimization of the I_p ramp-up with an early L-H transition needed to realize low-l_i and high elongation H-mode discharges when NSTX-U operations resume.

Wall conditioning for the initial commissioning phase was provided by a high-temperature bake of the graphite walls, inter-shot glow discharge cleaning (GDC) and boronizations. Weekly boronizations were completed during the first seven weeks before switching to smaller, nightly boronizations. While the nightly (i.e. mini) boronizations were successful in maintaining the oxygen content of the plasmas at an acceptable level, the thinner coatings led to a faster degradation of the wall conditions and reduced the reproducibility of H-mode discharges. Modifications to the inner divertor are being pursued prior to the next experimental campaign in order to improve the bake of the inner divertor. In addition, future operations will employ between-shot lithium wall conditioning, which was observed on NSTX to provide beneficial and reproducible wall conditions.

Much of the progress in the commissioning phase was enabled by excellent availability of the plasma diagnostics. Operations relied heavily on the Thomson scatting system, fast cameras and filterscope systems that were operational from first plasma. Within the first two weeks of operation, NSTX-U was producing H-mode discharges with between-shot equilibrium calculations constrained by Thomson scattering measurements of the electron density and temperature. A number of new diagnostics that supported the experiments on NSTX-U were commissioned, including the real-time velocity (RTV) CHERS diagnostics and the materials analysis and particle probe (MAPP).

NSTX-U had a productive commissioning period and is poised to quickly address key scientific issues when operations resume. About 90% of the planned commissioning activities were competed in ten weeks of operations. Two significant activities that were started but not completed were the measurement of the current profile using MSE diagnostics and the implementation of real-time resistive wall mode (RWM) identification and correction. A number of activities are being pursued in parallel with the replacement of the PF1AU coil that prompted the early conclusion of the commissioning phase. One such activity is a modification of the divertor region in order to achieve higher bake out temperatures on the inner divertor and simplify the vacuum boundary. Also, the activities that were planned for the conclusion of the first experimental campaign are proceeding, including the installation of new diagnostics and changes to the device required for achieving $I_p = 2$ MA and $B_T = 1$ T operation.

Acknowledgements

The authors thank the NSTX-U Research, Operations and Engineering teams for their persistent and dedicated efforts. This work was supported primarily by the US DOE under Contract DE-AC02-09CH11466. Portions of this research were performed under the auspices of the US DOE by Lawrence Livermore National Laboratory under Contract DE-AC52-07NA27344. The digital data for this paper can be found in: http://arks.princeton.edu/ark:/88435/dsp011v53k0334.

1 Ono M. *et al* 2002 *Nucl. Fusion* **40** 557

2 Sabbagh S.A. *et al* 2013 *Nucl. Fusion* **53** 104007

3 Menard J.E. *et al* 2012 *Nucl. Fusion* **52** 083015

4 Ono M. *et al* 2015 *Nucl. Fusion* **55** 73007

5 Gerhardt S.P., Andre R. and Menard J.E. 2012 *Nucl. Fusion* **52** 83020

6 Menard J.E. *et al* 2016 *Nucl. Fusion* **56** 106023

7 Menard J.E. *et al* 2011 *Nucl. Fusion* **51** 103014

8 Boyer M.D. *et al* 2015 *Nucl. Fusion* **55** 53033

9 Goumiri, I. R. *et al* 2016 *Nucl. Fusion* **56** 36023

10 Boyer M. D. *et al* 2017 *Nucl. Fusion* **57** 66017

11 Fredrickson E.D. *et al* 2017 *Phys. Rev. Lett.* **118** 265001

12 Soukhanovskii V.A. *et al* 2016 *IEEE Trans. Plasma Sci.* **44** 3445

13 Menard J.E. *et al* 2017 *Nucl. Fusion* **57** 102006

14 Que W. *et al* 2015 *IEEE 26th Symposium on Fusion Engineering (SOFE)*

15 Sabbagh S.A. *et al* 2010 *Nucl. Fusion* **50** 25020

16 Ramakrishnan S. *et al* 2013 *IEEE 25th Symposium on Fusion Engineering (SOFE)*

17 Erickson K.G., Tchilinguirian G.J., Hatcher R.E. and Davis W.M. 2014 *IEEE Trans. Plasma Sci.* **42,** 1811

18 Erickson K.G. *et al* 2014 *Fusion Eng. Des.* **89** 853

19 Gerhardt S.P. *et al* 2014 *Rev. Sci. Instrum.* **85** 11E807

20 Sabbagh S.A. *et al* 2001 *Nucl. Fusion* **41** 1601

21 Sabbagh S.A. *et al* 2006 *Nucl. Fusion* **46** 635

22 Diallo A., Leblanc B.P., Labik G. and Stevens D. 2012 *Rev. Sci. Instrum.* **83** 10D532

23 Bell R.E. *et al* 2010 *Phys. Plasmas* **17** 082507

24 Biewer T.M., Bell R.E., Feder R., Johnson D.W. and Palladino R.W. 2004 *Rev. Sci. Instrum.* **75** 650

25 Podestà M. and Bell R. E. 2012 *Rev. Sci. Instrum.* **83** 033503

26 Bell R.E. and Feder R. 2010 *Rev. Sci. Instrum.* **81** 10D724

27 Soukhanovskii V.A., Johnson D.W., Kaita R. and Roquemore A.L. 2006 *Rev. Sci. Instrum.* **77** 10F127

28 Scotti F., Roquemore A.L. and Soukhanovskii V.A. 2012 *Rev. Sci. Instrum.* **83** 10E532

29 Scotti F. and Soukhanovskii V.A. 2015 *Rev. Sci. Instrum.* **86** 123103

30 Bedoya, F. *et al*. 2017 *Nucl. Mater. Energy* **12** 1248

31 Tritz K., Clayton D.J., Stutman D. and Finkenthal M. 2012 *Rev. Sci. Instrum.* **83** 10E109

32 Kumar, D. *et al*. 2010 *Rev. Sci. Instrum.* **81** 10E507

33 Soukhanovskii V.A., Roquemore A.L., Bell R.E., Kaita R. and Kugel H.W. 2010 *Rev. Sci. Instrum.* **81** 10D723

34 Vann R.G.L., Brunner K.J., Ellis R., Taylor G. and Thomas D.A. 2016 *Rev. Sci. Instrum.* **87** 11D902

35 Weller M.E., Beiersdorfer P., Soukhanovskii V.A., Magee E.W. and Scotti F. 2016 *Rev. Sci. Instrum.* **87** 11E324

36 Stotler D.P. *et al* 2015 *Phys. Plasmas* **22** 82506

37 Liu D. *et al* 2016 *Rev. Sci. Instrum.* **87** 11D803

38 Skinner C.H. *et al* 2017 *Nucl. Mater. Energy* **12** 744

39 Maingi R. *et al* 2015 *J. Nucl. Mater.* **463** 1134

40 Lloyd B. *et al*. 1991 *Nucl. Fusion* **31** 2031

41 Tanga A., Thomas P.R., Cordey J.G. *et al* in Tokamak Start-up (Knoepfel, H., Ed.), Plenum Press, New York (1986) 159

42 Menard J.E. *et al* 2010 *Nucl. Fusion* **50** 45008

43 Lazarus E.A., Lister J.B. and Neilson G.H. 1990 *Nucl. Fusion* **30** 111

44 Soukhanovskii V.A. *et al* 2003 *J. Nucl. Mater.* **313–316,** 573–578

45 Gerhardt S.P. *et al* 2013 *Nucl. Fusion* **53** 63021

46 Gates D.A. *et al* 2006 *Fusion Eng. Des.* **81** 1911

47 Boyer M.D. *et al* 2017 *Nucl. Fusion* (submitted)

48 Ferron J. *et al* 2002 *Nucl. Fusion* **38** 1055

49 Gates D.A. *et al* 2006 *Nucl. Fusion* **46** 17

50 Gerhardt S.P. *et al* 2014 *Rev. Sci. Instrum.* **85** 11E807

51 Myers, C. *et al*. "Initial error field correction studies in the National Spherical Torus Experiment Upgrade." *APS (2016)*

52 Menard J.E. *et al* 2003 *Nucl. Fusion* **43** 330

53 Gerhardt S.P. *et al* 2010 *Plasma Phys. Control. Fusion* **52** 104003

54 Buttery R. *et al* 1999 *Nucl. Fusion* **39** 1827

55 Scoville J.T. and La Haye R.J. 2003 *Nucl. Fusion* **43** 250

56 Park J.-K. Boozer A.H. and Glasser A.H. 2007 *Phys. Plasmas* **14** 052110

57 Ferraro N.M., Jardin S.C., Lao L.L., Shephard M.S. and Zhang F. 2016 *Phys. Plasmas* **23** 056114

58 Guttenfelder W. *et al* 2017 Nuclear Fusion *submitted*

59 Menard J.E *et al* 2002 *Nucl. Fusion* **41** 1197

60 Gates D.A. *et al Nucl. Fusion* **46** S22

61 Sabbagh S.A. *et al* 2004 *Nucl. Fusion* **44** 560

62 Maingi, R. *et al* 2005 *Nucl. Fusion* **45** 1066

63 Sontag A.C. *et al* 2011 *Nucl. Fusion* **51** 103022

64 Berkery J.W., Sabbagh S.A., Bell R.E., Gerhardt S.P. and LeBlanc B.P. 2017 *Phys. Plasmas* **24** 056103

65 Kaye S. *et al* 2006 *Nucl. Fusion* **46** 848